

Filamentogenesis and Filamentolysis of a ~~Light-Filament~~Low-density filament: Dynamic Processes in the Near-Surface Ocean Under Tidal Forcing

Michelle Albinus¹, Thomas H. Badewien¹, Lisa Gassen², Oliver Wurl² and Jens Meyerjürgens¹

¹Carl von Ossietzky Universität, Institute for Chemistry and Biology of the Marine Environment, Marine Sensorsystems, Oldenburg, Germany.

²Carl von Ossietzky Universität, Institute for Chemistry and Biology of the Marine Environment, Processing and Sensing of Marine Interfaces, Oldenburg, Germany.

Correspondence to: Michelle Albinus (michelle.albinus@uol.de), Jens Meyerjürgens (jens.meyerjuergens@uol.de)

Abstract. This study investigates the dynamics and evolution of a low-density filament driven by freshwater-induced buoyancy ~~light-filament~~low-density filament embedded within a tidal mixing front, focusing on its spatial and temporal evolution in the near-surface layer (0.1 - 10 m) of the water column. A high-resolution, multi-sensor synoptic dataset, consisting of surface drifters, a drifting sensor chain, and an autonomous surface vehicle equipped with an Acoustic Doppler Current Profiler, temperature, and conductivity sensors, was used to observe patterns of divergence, vorticity, and vertical velocities, avoiding high temporospatial aliasing. The measurements resolved three phases of the filament occurring on length scales of O(0.1-2 km) and time scales of minutes to one hour: I) establishment of the filament in the overlying first meter and filamentolysis < 1 m, II) the ongoing filamentolysis in the lower NSL induced filamentogenesis above 0.6 m, III) restratification of the upper 0.6 m. Vertical velocities ranged between $\pm 20 \text{ m d}^{-1}$ with pronounced asymmetric responses on the filament boundaries due to the coupling of filamentary and tide-induced vertical motions. In phase III, stratification allowed for increased heat uptake within the filament. These investigations highlight the role of the overlooked top surface layer in potentially altering the energy, heat, and gas budget of the ocean, which is critical for understanding the air-sea interface in the context of climate change.

1 Introduction

Light-Low-density filaments, narrow, buoyant intrusions of warm or less dense water into denser surroundings, are a rarely observed but dynamically significant manifestation of frontal activity in shelf seas. They form when frontal geometry, background flow, and strain orientation combine to elongate and pinch meanders into streamer-like features (Thomas et al., 2008). The strain field determines which side of the front is drawn out: when dense water extends into lighter water, a cold/dense filament forms, reinforced by upwelling from ageostrophic secondary circulation (ASC; McWilliams, 2009; 2015). In contrast, ~~light-filament~~low-density filaments arise when buoyant water intrudes into denser regions, typically in anticyclonic strain zones or via eddy-front interactions. These features are short-lived: ASC downwelling subducts the buoyant anomaly beneath the mixed layer, while local stratification suppresses vertical replenishment, making lateral

advection essential for their persistence (Jakes et al., 2023). Their horizontal scales are located between the mesoscale regime and small-scale three-dimensional turbulence (Chrysagi et al., 2021) with a vertical extent to the upper 50 m of the surface ocean (Thomas and Lee, 2005; Mahadevan and Tandon, 2006). Vertical velocities driving ASC may reach $\pm 100 \text{ m d}^{-1}$, restratifying horizontal density gradients within subinertial time scales (Thomas and Lee, 2005; Chrysagi et al., 2021). Such asymmetries in formation and lifetime render ~~light filament~~low-density filaments both dynamically important and observationally elusive. Those findings apply well to dense/cold filaments that are investigated within various studies (e.g. McWilliams, 2009; Johnson et al., 2020; Chrysagi et al., 2021; Esposito et al., 2023). Some of them state the occurrence of low-density filaments and Lapeyre and Klein (2006) underscore the importance of filamental upwelling as develops at low-density filaments for the ocean nutrient flux. McWilliams (2015) points to the rarity of low-density filaments, but otherwise frontal literature lacks a quantification from either models and in situ observations of this type of filaments.

The southern North Sea provides an ideal setting to study these processes. There, tides, wind forcing, and freshwater input create a highly energetic and deformable frontal environment. Tidal mixing fronts (~~TMFs~~) form at the interface between vertically stratified and well-mixed waters in summer, when surface heat flux steepens lateral temperature gradients (Van Heijst, 1986). ~~TMFs~~Those fronts occur on continental shelves worldwide (Timko et al., 2019) and mediate exchanges of nutrients, particles, and energy between ocean layers (Thomas et al., 2008; Sun and Cho, 2010). In the North Sea, TMFs vary seasonally under semidiurnal tides, fortnightly spring–neap cycles, bottom topography, and intermittent winds (Simpson et al., 1990; Holt and Umlauf, 2008; Zhao et al., 2019). Especially in the southern North Sea, freshwater input from rivers can lower coastal salinity by up to $10 \text{ g}\cdot\text{kg}^{-1}$ (Chegini et al., 2020), steepening density gradients and intensifying fronts (Simpson et al., 1990; Ricker et al., 2021; Goßmann et al., 2025). According to Núñez-Riboni and Akimova (2017) river-runoff is responsible for $\sim 80\%$ of the inter-annual salinity variability in the southern North Sea, both in terms of spatial extent and magnitude. Chegini et al. (2020) estimated the combined freshwater flux of the rivers Elbe, Weser, Ems and Eider to be $1200 \text{ m}^3\text{s}^{-1}$, however, Meyer et al. (2025) state that the river Elbe can afford a freshwater input up to $\sim 1420 \text{ m}^3\text{s}^{-1}$ alone in winter season. The additional freshwater mainly remains in the upper water column, forming a two-layer stratification (Stanev et al., 2015). This state persists depending on the freshwater flux added; Chegini et al. (2020) recorded a massive Elbe-runoff event ($>4000 \text{ m}^3\text{s}^{-1}$) causing a continuous stratification in shallow waters (20–30 m; near the island of Helgoland) in summer 2013 that lasted 120 days. In combination with semidiurnal tides with tidal hubs exceeding $\sim 3.5 \text{ m}$ (Meyer et al., 2025), an overturning estuarine circulation forms, where low-density surface water flows seawards and denser North Sea water propagates landwards near the bottom, oscillating with mixing during periods (Burchard and Badewien, 2015). Stanev et al. (2015) explain salinity to be responsible for 20% of this overturning circulation, with the remaining drivers being winds, external salinity input (precipitation, inflow from adjacent seas and channels; Núñez-Riboni and Akimova, 2017). These cumulative processes and preconditions acting on horizontal density gradients, make fronts in the North Sea highly sensitive to mesoscale and submesoscale strain, a key prerequisite for

~~frontogenesis (Garcia-Jove et al., 2022). Freshwater from rivers such as the Elbe can lower coastal salinity by up to 10 g kg^{-1} , steepening density gradients and intensifying fronts (Simpson et al., 1990; Ricker et al., 2021; Goßmann et al., 2025). Shallow bathymetry amplifies these effects, making TMEs highly sensitive to mesoscale and submesoscale strain, a key prerequisite for frontogenesis (Garcia Jove et al., 2022).~~

~~divergent flow (divergence) drives upward motion on the light side and convergent flow (convergence) downward motion on the dense side, flattening isopycnals and enhancing stratification, whereas reversed patterns lead to frontolysis. Analogous dynamics occur in narrow buoyancy filaments, where horizontal strain sharpens buoyancy gradients and drives ASC, a process referred to as filamentogenesis (McWilliams, 2009, 2015; Garcia-Jove et al., 2022; Jakes et al., 2023). This circulation acts to restore stratified balance but modifies the filament structure depending on its buoyancy anomaly: dense filaments are reinforced by surface convergence and central downwelling that deepen the anomaly to several hundred meters (e.g., Garcia-Jove et al., 2022), whereas low-density filaments experience reversed circulation that shoals buoyant water toward the surface (Thomas et al., 2008) and promotes rapid filament decay. In this study, “filamentogenesis of low-density filaments” is defined as the ASC-driven adjustment process acting on buoyant filaments, in which reversed circulation transports light water upward and outward, shoaling the buoyancy anomaly and leading to rapid filament weakening and decay as stratification is restored. During frontogenesis, ASC drives upward motion on the light side and downward motion on the dense side, flattening isopycnals and enhancing stratification, while reversed ASC leads to frontolysis (McWilliams, 2009; Chrysagi et al., 2021; Garcia Jove et al., 2022). Similar dynamics govern filaments, referred to as filamentogenesis and filamentolysis (e.g., McWilliams 2009, 2015; Garcia Jove et al., 2022; Jakes et al., 2023). Dense filaments are reinforced by ASC driven convergence, while light filaments experience reversed circulation, promoting rapid decay. Further, dense filaments can extend down several hundred meters (e.g., Garcia Jove et al., 2022), while light filaments are rather pronounced at the ocean surface (Thomas et al., 2008). Capturing these dynamics requires high-resolution measurements and calculation of Differential Kinematic Properties (DKP), such as divergence, vorticity, and horizontal velocity gradients, from water-column instabilities or path-integrated velocity gradient quantities parcel deformation (e.g., Vélez-Belchí and Tintoré, 2001; Molinari and Kirwan, 1975; Berta et al., 2016; Huntley et al., 2022). Surface drifters, HF radar, and ADCPs have been widely used (e.g., Hill et al., 1993; Shcherbina et al., 2013; Berta et al., 2016, Archer et al., 2020; Esposito et al., 2023), yet most studies lack data from the uppermost meter of the ocean, precisely where frontal and light filament/low-density filamentary processes peak (Thomas et al., 2008; Chrysagi et al., 2021; Gassen et al., 2023). Submesoscale features ($O[0.1-10 \text{ km}]$) are critical for the ocean’s energy cascade, both distributing energy forward and feeding larger scales (Schubert et al., 2020; Zhang et al., 2023). In shallow seas like the North Sea, these processes are assumed to be strongly imprinted at the surface, yet high-resolution observations remain scarce and temporally aliased (Johnson et al., 20204).~~

Building on this gap, we suggest that high freshwater contrasts in the southern North Sea generate the conditions necessary for low-density filament formation. Tidal oscillations may favour the export of dense filaments offshore into denser surroundings and alter filaments by alternately shearing, stretching, and compressing the density field. ~~we suggest that tidal oscillations in the southern North Sea, by alternately shearing, stretching, and compressing the density field, may occasionally generate the conditions necessary for light filament formation. While tidal reversals may favour the export of dense filaments offshore, phases where tidal flow and wind-driven advection align may instead pull buoyant surface water into denser surroundings.~~ In these situations, transient anticyclonic strain zones can develop along the front, momentarily reversing the usual dense-offshore export and enabling warm-side water to intrude into the cold side. Although such ~~light filament~~ low-density filament events are rare and short-lived, the unique tidal environment of the southern North Sea offers occasional opportunities to capture them. To test this hypothesis, we conducted high-resolution ADCP and CTD measurements at O[0.1-2 km] scales using an autonomous surface vehicle (ASV) at a ~~TMP-tidal mixing front~~ in the southern North Sea. Trajectories from 14 surface drifters and a drifting sensor chain complemented these observations, resolving the evolution of a ~~light filament~~ low-density filament with a focus on the near-surface layer (NSL; 0.1-10 m). This dataset allows us to ~~characterize the buoyancy-driven nature of the filament and the role of tidal modulation in amplifying and weakening its surface divergence signal, the mechanisms of rapid filament development, surface expression, and decay,~~ providing new insight into these elusive but dynamically important features.

2 Materials and Methods

2.1 Data acquisition

During cruise HE626 on RV Heincke, ~~we collected~~ a multi-platform dataset combining ship-based, autonomous, and Lagrangian observations was collected. Central to the study were measurements by the ASV Halobates (Wurl et al., 2024), which provided current velocities in the NSL as well as high-resolution temperature and salinity profiles. Additional underway observations included wind data and continuous NSL hydrographic measurements (temperature and conductivity) from a 4H Jena Engineering Pocketbox Ferrybox flow-through system. Stationary measurements consisted of ship-based Seabird SBE911+ CTD casts and deployments of Lagrangian platforms, including 14 near-surface drifters (Meyerjürgens et al., 2019) and a drifting sensor chain. The focus of this study is on observations from 5 August 2023, northwest of Helgoland (Fig. 1a), targeting submesoscale frontal processes under freshwater input from the Weser and Elbe estuary and strong semidiurnal tidal influence. The region was characterized by ~~TMP-tidal mixing front~~ structures on scales of O(0.1-10 km), visible in sea surface salinity (SSS). The more saline water mass originated from the open North Sea, while the fresher mass consisted of a mixture of North Sea water and river runoff from the German Bight (Burchard and Badewien, 2015). Semidiurnal tides imported saline offshore water, creating horizontal gradients of up to $\pm 1.5 \text{ g}_{-}\text{kg}^{-1}$ (Fig. 1a). The frontal

130 | system exhibited submesoscale meanders (Fig. 1a) and developed a ~~light filament~~low-density filament on horizontal scales of 0.1-2 km (Fig. 1c).

135 | Front detection was Front detection was performed by observing satellite-based sea surface foundation temperature (CMEMS, 2023) and guided by SSS fields from the CMEMS Atlantic-European Northwest Shelf Ocean Physics Analysis and Forecast model (CMEMS, 2024), which has a horizontal resolution of ~~$\sim 3 \text{ km} \times 3 \text{ km}$~~ $0.027^\circ \times 0.027^\circ$ and hourly output. For the target region, model SSS correlated reasonably with in situ Ferrybox salinity ($R = 0.71$; Fig. B1). On the evening of 4 August, the vessel carried out a zig-zag survey ($\sim 7 \text{ kn}$) to validate the model fields and identify the strongest gradient, which reached $\Delta \text{SSS} \approx 1.2 \text{ g}\cdot\text{kg}^{-1}\cdot\text{km}^{-1}$. In situ salinity was obtained from the Ferrybox, pumping seawater from 3 m depth ($\sim 6 \text{ L}\cdot\text{min}^{-1}$) with conductivity measurements accurate to $\pm 0.3 \text{ mS}\cdot\text{cm}^{-1}$. Once the gradient was confirmed, the vessel remained on
140 | station to deploy the Lagrangian instruments. A sensor chain equipped with six Sea&Sun CTM 48M CTDs mounted between 0.2-10 m depth, transmitting position data every 2 min (Garmin inReach Messenger GPS), and 14 surface drifters transmitting positions every 5 min (SPOT Trace® GPS). The drifters were deployed by zodiac in the form of 12 triangular arrays (Fig. 1b) and tracked over 25 h. Their trajectories showed a north-westward drift under prevailing southeasterly winds (Fig. C12), covering $\sim 21 \text{ km}$, while their rotary motion reflected tidal currents (Meyerjürgens et al., 2020). During ebb tide,
145 | drifters were displaced westward at speeds up to $1 \text{ m}\cdot\text{s}^{-1}$, an effect intensified by wind forcing between 14:00-21:00 UTC when wind speeds increased from 6 to $14 \text{ m}\cdot\text{s}^{-1}$. The sensor chain largely followed the drifter displacement.

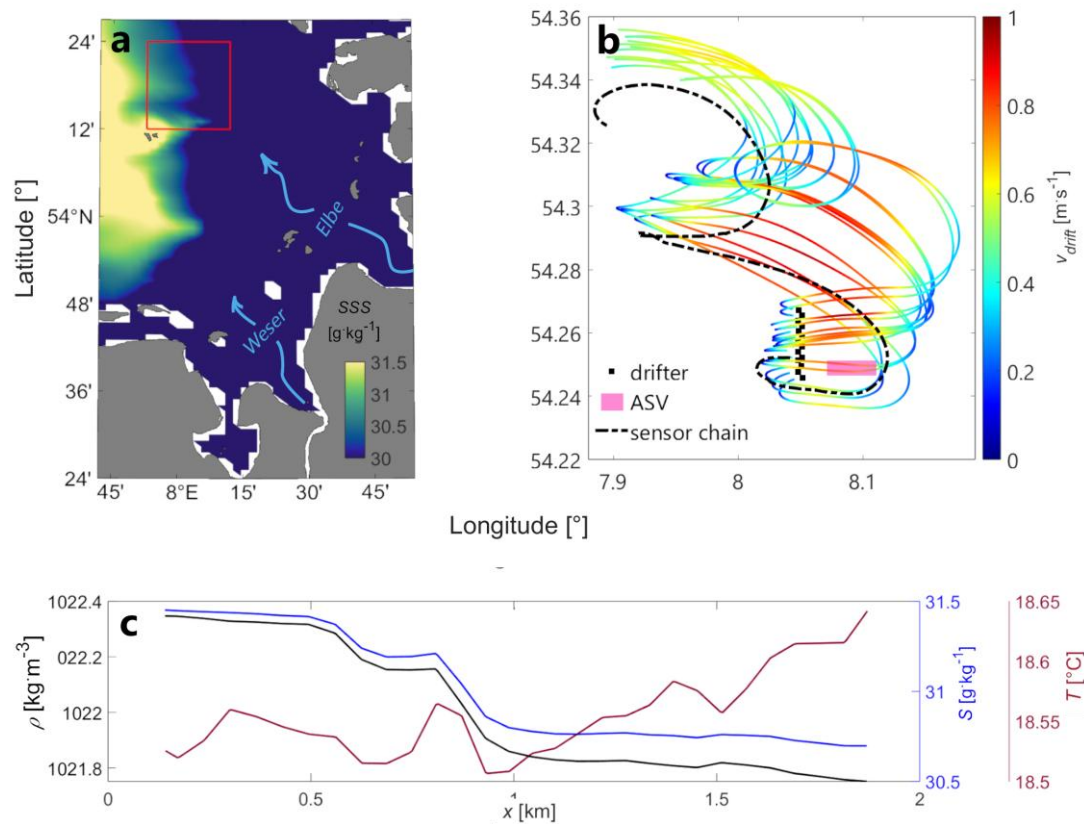


Figure 1. a) The study site is located in the southern North Sea, northeast of Helgoland, highlighted with a red box. On August 5th, 2023, the area exhibits submesoscale structures (low-density filament) with SSS gradients of $\pm 1.5 \text{ g} \cdot \text{kg}^{-1} \cdot \text{km}^{-1}$. b) Measurements within the red box include a drifting sensor chain (black dot-dashed line), 14 Lagrangian surface drifter deployments (initial positions as black squares) and the ASV (pink area). Drifter trajectories are colored by current velocity magnitude. c) Density (black line), salinity (blue line) and temperature (red line) of the filament sampled by the ASV.

After the Lagrangian deployments, the ASV ~~HALOBATES (Wurl et al., 2024)~~ was launched within the frontal zone to observe the propagation of the ~~light filament~~low-density filament at high temporal resolution. The vehicle executed a repeating rectangular track ($\sim 2 \text{ km}$ east-west, 0.08 km north-south), with only the east-west transects analyzed (Fig. 1c). Seven transects were completed between 06:30 and 12:45 UTC at $\sim 2 \text{ kn}$. The ASV carried a Teledyne RD Instruments RiverRay 600 kHz ADCP, mounted at 0.275 m immersion depth. With a 1 m vertical bin size, velocity profiles were

160 obtained from 1-10 m depth (excluding near-bottom bins). Thus, ADCP data began at 1 m and extended through the NSL,
but did not cover the overlying surface layer. In contrast, the ASV was equipped with seven Itronaut OS310 CTDs mounted
at 80-100 μm (denoted the skin layer; Shinki et al., 2012), 30 cm, 40 cm, 50 cm, 60 cm, 85 cm, and 100 cm. Those resolved
temperature and salinity changes within the skin layer down to one meter of the water column, allowing the evolution of the
filament surface expression to be captured in detail. HALOBATES-The ASV is equipped with rotating glass plates that pick
165 up the skin layer by surface tension followed by scrapes transferring the water into the tube system being connected to the
CTDs. Because of this setup, the CTDs and ADCP provided complementary rather than overlapping coverage: CTDs
focused on the upper meter, while the ADCP recorded current velocities in the deeper part of the NSL.

For analysis, ADCP data were filtered to remove outliers ($>3\sigma$ from the mean), truncated below 10 m depth, and smoothed
170 using a 60 s moving average. Drifter positions were post-processed following Deyle et al. (2024), yielding interpolated
trajectories with a uniform 5 min resolution, including bridging of GPS gaps up to 1 h.

2.2 Surface divergence from drifters

A variety of studies have estimated divergence by tracking the deformation of drifter clusters (Molinari and Kirwan, 1975;
175 Kawai, 1985; Berta et al., 2016; Tarry et al., 2021; Huntley et al., 2022; Esposito et al., 2023). Molinari and Kirwan (1975)
introduced two robust approaches: (a) the method of least squares, which infers divergence from velocity gradients fitted
around the cluster centroid, and (b) the area-based method, which calculates divergence from the rate of change in the
polygonal area spanned by a drifter group. While the least-squares method scales well to larger clusters and offers higher
statistical confidence (Molinari and Kirwan, 1975; Tarry et al., 2022), it requires more drifters and is sensitive to tidal
180 modulation of trajectories, which can obscure frontal signatures. The area-based method is less demanding, relying on only
three drifters, and is therefore better suited for frontal environments where deformation rates are high. In this study, we
applied the latter, expressed as

$$\delta = \frac{1}{A} \frac{\partial A}{\partial t} \quad (1)$$

185 where A is the area of a drifter triplet and $\partial A/\partial t$ its temporal change.

To maximize the number of usable triplets, drifters were deployed on 5 August 2023 as vertices of 12 potential triangles with
edge lengths of 0.2-0.5 km along a ~ 4 km transect (Fig. 1b). Only complete triplets were retained, excluding 21.8% of
190 deployments with <3 drifters. Because high-gradient fronts coincide with elevated strain rates (Mahadevan and Tandon,
2006), clusters in such areas were particularly prone to rapid elongation and biased divergence estimates. To address this,

Berta et al. (2016, 2020) and Huntley et al. (2022) proposed quality metrics that characterize triangle geometry. One such measure is

195
$$\Lambda = \frac{12\sqrt{3}A}{P^2} \quad (2)$$

where P is the perimeter. $\Lambda = 1$ corresponds to equilateral triangles, while $\Lambda = 0.2$ indicates near-collinear configurations. Huntley et al. (2022) demonstrated that Λ provides slightly more reliable results than internal-angle metrics (θ, γ), with ~4 % better accuracy. Given the limited sample size (~20 triplets per time step), this improvement was significant. Applying a conservative filter of $0.2 \leq \Lambda \leq 1$ retained 36.4 % of the available clusters, leaving 3559 valid triplets for divergence estimation. Overlaps in drifter trajectories in highly dynamic regimes (e.g., tidal transitions or wind-driven surges; Fig. 2b) further reduced the number of suitable triplets (Berta et al., 2016; Villa Castrillón et al., 2024).

205 Divergence was then calculated for each triplet centroid using equation (1). Triplets were time-binned according to tidal phase, since tidal reversals prevented uniform resampling ([calculation of divergence from clusters every 15 min; Esposito et al., 2023](#)). Five intervals were identified (t₁-t₅: 1.5, 5, 7.5, 5.5, 5.5 h), [this study however, focuses on t₂ as this was the period for detecting the low-density filament](#). Delaunay triangulation at the start of each interval increased usable triplets and avoided configurations already deformed. Divergence estimates were subsequently gridded onto a 1 × 1 km grid, averaging values within each spatial bin and time interval. This yielded 2179 triplets suitable for analysis. Finally, divergence values
210 were normalized by the Coriolis frequency $f = 1.18 \times 10^{-4} \text{ s}^{-1}$ at a reference latitude of 54.25 °N.

2.3 Water column properties and instabilities from drifting sensor chain and ASV CTDs

Since the sensor chain trajectory broadly followed the drifters, it provided an additional basis to investigate water column structure and instabilities at the front. ~~To compare with the drifter derived divergence field, divergence was also estimated from the chain trajectory. Coordinates were first smoothed with a 10 min moving average to reduce noise, and divergence δ was then calculated as~~

~~$$\delta = \frac{\partial u}{\partial x} - \frac{\partial v}{\partial y} \quad (3)$$~~

220 ~~where u and v are the cross- and along-front velocity components, obtained by rotating earth-referenced velocities into the chain's azimuthal frame. As before, δ was normalized by the Coriolis frequency f .~~

To characterize the water masses shaping the front, temperature and conductivity from the chain sensors were converted to conservative temperature, absolute salinity, and in-situ density at depths $z = [0.2, 1.2, 6.2, 8.4, 10.6]$ m. The same procedure

Formatiert: Block

Formatiert: Standard, Zeilenabstand: einfach

was applied to the ASV CTD data at depths $z = [0.0001, 30, 40, 50, 60, 85, 100]$ cm. These profiles were then used to derive water column instability proxies: the Brunt-Väisälä frequency

$$N^2 = \frac{\partial b}{\partial z}, \quad (34)$$

and the lateral buoyancy gradient

$$M^2 = \frac{\partial b}{\partial x}, \quad (45)$$

with buoyancy defined as $b = g(1 - \rho / \rho_0)$, where ρ is potential density and $\rho_0 = 1022.3 \text{ kg m}^{-3}$ is the surface reference density. By examining the evolution of isopycnal slopes, periods of restratification and mixing could be identified.

2.4 Divergence from ASV-mounted ADCP

To investigate frontal dynamics at the lower end of the submesoscale and at high temporal resolution, divergence was also calculated from the ADCP mounted on the ASV. Following Rudnick (2001), the assumption of a frontal jet aligned with the front allows of the full divergence term $\delta = \frac{\partial u^*}{\partial x} + \frac{\partial v^*}{\partial y}$ (where u^* and v^* are the cross- and along-front velocity components) to equation (3) to be simplified to

$$\delta \approx \frac{\partial u}{\partial x}, \quad (56)$$

a formulation commonly known as the “one-ship method” (Shcherbina et al., 2013). This approach has been widely applied to ADCP data for single-depth divergence estimates (e.g., Drinkwater and Loder, 2001; Archer et al., 2020; Esposito et al., 2023).

From the ASV-mounted ADCP, the along-track velocity component was extracted and organized into transects (Fig. 1c). Data were averaged onto a grid with 10 m horizontal spacing, 2 min temporal resolution, and 1 m vertical intervals before applying equation (56), and the resulting divergence estimates were normalized by the Coriolis frequency f . To capture the temporal evolution of the low-density filament at TMF, full-depth transects were analyzed at three times during the morning sequence ($t_1 = 07:23$, $t_2 = 07:40$, $t_3 = 08:30$). (~~07:23, 07:40, 08:30~~). In addition to horizontal divergence, the vertical component of relative vorticity,

$$\zeta = \frac{\partial v}{\partial x} - \frac{\partial u}{\partial y}, \quad (67)$$

255 was derived using the same method, together with the along-front velocity v , to characterize the jet structure. Surface density transects from the ASV CTD at $z = 1$ m were analyzed for the same times, alongside co-located depth sections of δ , ζ , and v . Vertical velocity fields were overlaid to highlight frontogenesis and frontolysis processes (see Section 2.5).

2.5 Vertical velocity from drifter and ADCP divergence estimates

260

Since horizontal divergence was used to diagnose vertical motion, vertical velocities in the water column were derived from the continuity equation,

$$\frac{\partial u}{\partial x} + \frac{\partial v}{\partial y} + \frac{\partial w}{\partial z} = 0, \quad ,$$

265 which can be rearranged to

$$\Delta w = - \int_{-z}^{z_0} \left(\frac{\partial u}{\partial x} + \frac{\partial v}{\partial y} \right) dz, \quad (78)$$

270 where Δw is the vertical velocity difference between the surface (z_0) and depth z . For drifters, the target depth was set to $z = -0.5$ m, corresponding to the drifter's immersion depth (Meyerjürgens et al., 2019). At the surface, previous studies (Tarry et al., 2021; Rypina et al., 2021; Tarry et al., 2022; Esposito et al., 2023) assumed $w(z_0 = 0) = 0$ m d⁻¹, as vertical motion at the surface is typically one to two orders of magnitude smaller than observed subsurface velocities. Rypina et al. (2021) argued that sea surface displacement is largely governed by gravity and tidal waves, yielding negligible vertical motion in the Mediterranean. In contrast, the North Sea exhibits much larger tidal amplitudes. Around Helgoland, the M2 tide causes vertical displacements of ~ 1.5 m (Stanev et al., 2014), making the tidal-induced vertical velocity at the surface comparable to observed w . Thus, the assumption $w(z_0 = 0) = 0$ m d⁻¹ was not valid here. Instead, sea surface height (SSH) with a root-mean-square difference (RMSD) of $\sim 5 - 15$ cm from CMEMS model data (2024) was used to estimate tidal vertical velocities at z_0 , applied as hourly means. For ADCP data, vertical velocities were calculated across the full depth range using equation (78). In this case, the one-ship method (equation 6) was substituted for the full divergence term, yielding:

280

$$w(z_i) = w(z_{i-1}) + \left(\frac{dw}{dz} \right) \Delta z, \quad (89)$$

where du/dx is the along-track divergence and Δz the ADCP bin size. A detailed derivation of equation (9) is provided in Appendix A. Since ADCP measurements begin at 1 m depth, tidal integration at the surface was unnecessary; the first estimate of w could be calculated directly at 2 m.

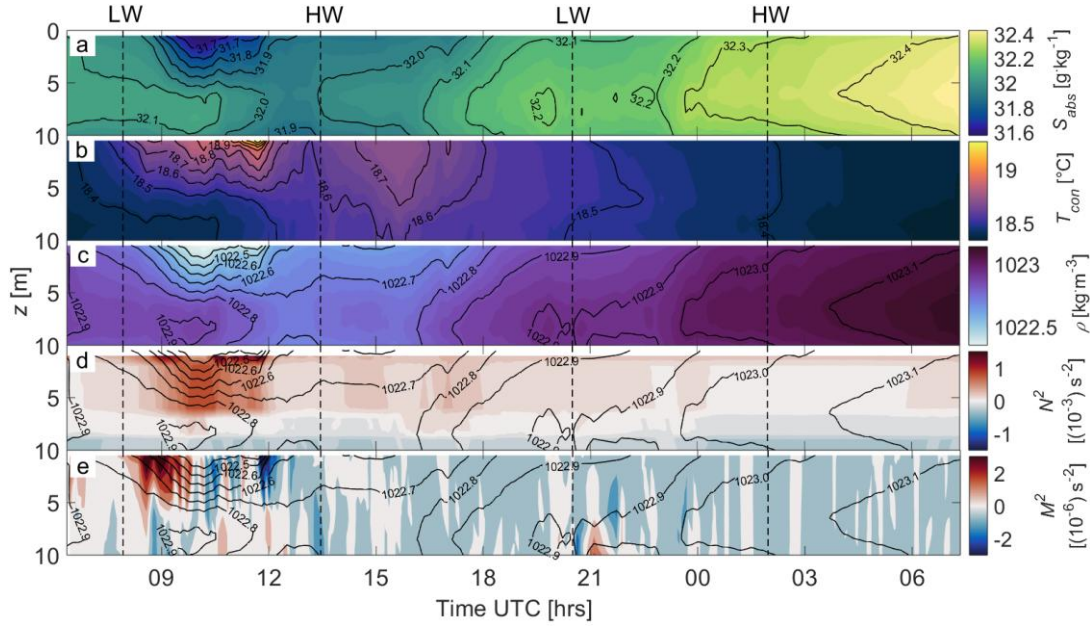
285

3 Results

3.1 Water column characteristics and instabilities from drifting sensor chain

290 | During the high tide period between 09:00 and 12:00, the sensor chain crossed the ~~light filament~~low-density filament, which was observed from the surface down to ~4–5 m and exhibited a density about 0.4 g kg^{-1} ~~lower than the surrounding TMF~~. It was embedded at the lower boundary of the TMF salinity signal ($\sim 31.5 \text{ g kg}^{-1}$) and at the highest boundary of the ~~TMF~~ temperature signal ($\sim 19.0 \text{ }^\circ\text{C}$), confirming its formation on the light side of the front, ~~as hypothesized~~. The filament persisted for approximately 3 h, showing a two-layer stratification from 09:00 to 12:00, with fresh (warm) water overlying more saline (cold) water. During the first two hours, the upper, lighter layer extended down to ~4 m and retreated to ~2 m in the final
295 | hour. This retreat was driven by a decrease in the salinity gradient while the temperature gradient increased (Fig. 2b,c). Around 17:00, the sensor chain crossed to the dense side of the TMF, where the filament was no longer apparent in salinity, temperature, or density.

300 | The filament also influenced water column stability, evident in the Brunt-Väisälä frequency (N^2) and lateral buoyancy gradient (M^2). The ~~light filament~~low-density filament emerged from the surrounding ~~TMF~~tidal mixing front as a region of strongly positive N^2 (Fig. 2d), indicating stable stratification. Below 7 m, negative N^2 values suggested local buoyancy production, likely caused by vertical shear acting on horizontal density gradients near the bottom, possibly due to tidal interactions with topography. This feature correlated with the bifurcation of isopycnals (“forking”), where dense water was forced over lighter water, a property appearing along the entire TMF time series rather than being unique to the filament.
305 | Considering the lateral buoyancy gradient (Fig. 2e), M^2 was positive (stable) when the filament was at ~4 m depth, but reversed to negative values during its retreat, indicating buoyancy production and the upward displacement of the filament, ~~as will be further discussed in a later section. This asymmetry will be further discussed in section 3.4.-~~



310 Figure 2. Time series of a) absolute salinity, b) conservative temperature, c) potential density, d) Brunt-Väissälä frequency N^2 and e) lateral buoyancy gradient M^2 obtained from the drifting sensor chain during August 5th and 6th. Vertical black dashed lines mark low water (LW) and high water (HW). N^2 and M^2 are displayed with overlain isopycnals. The low-density filament can be observed between the first LW and HW.

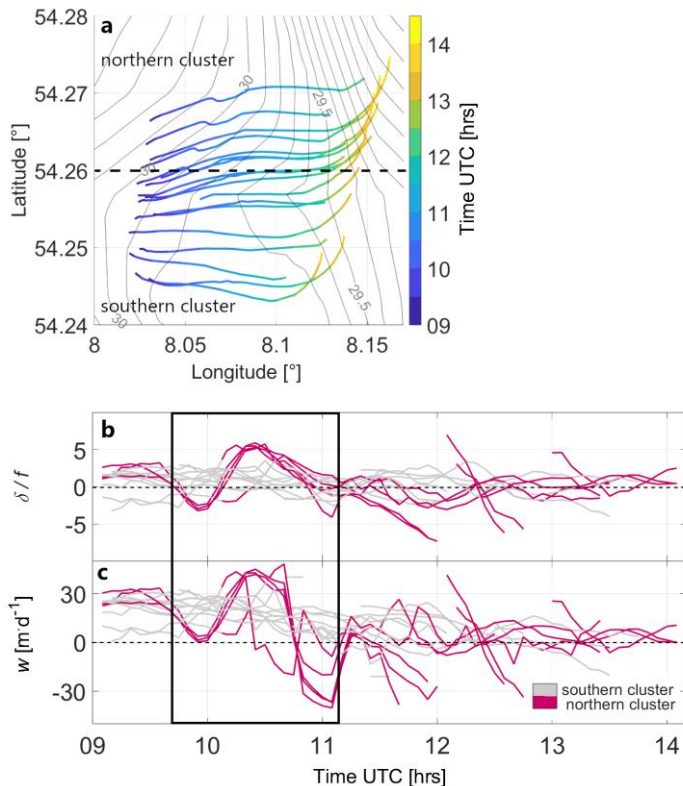
315

3.2 Coupling of filamentary and tide-induced vertical motions

320 Drifter triplet centroid trajectories from t2 over SSS isohalines (CMEMS, 2024, panel a) are shown in Figure 3 Figure 3 shows drifter triplet centroid trajectories over SSS isohalines (CMEMS, 2024, panel a), along with space- and time-binned near-surface horizontal divergence normalized by f (Fig. 3b) and vertical velocity w (Fig. 3c). As the drifters crossed TMF isohalines, these data reveal cross-front divergence and corresponding areas of up- and downwelling. Both SSS and drifter trajectories indicate that the TMF-tidal mixing front meandered on the mesoscale along the tidal wave direction, while a sudden southward diffraction of the northern trajectories around 8.05 °E longitude suggests a submesoscale light filament/low-density filament.

325

Following the main high tide current eastward (Fig. 3a), most drifters initially diverged with $\delta \approx 2f$ due to accelerating tidal flow (Fig. 3b, Fig. 1b). Shortly before 10:00, the northern cluster entered a convergence zone ($\sim -2f$), then peaked at $5f$ after ~ 30 min, and dropped to $-5f$ around 11:00. Although $\delta \approx \pm 5f$ is high relative to previous studies (Berta et al., 2016; Tarry et al., 2021, 2022), strong triplet deformation due to the tides likely caused overestimation (see section 2.2). Divergence drove **light filament/low-density filament** water upward away from the axis, while dense water sank during convergence (Fig. 3c), with vertical velocities ranging from $\sim -30 \text{ m d}^{-1}$ to 50 m d^{-1} . Despite potential overestimation due to error propagation from the divergence estimation ($\overline{\Delta\delta/f} \approx 2.928$), the vertical velocity pattern aligns with the drifter centroid trajectories, including the southward diffraction at 8.05 °E longitude. This behavior indicates the northern cluster sampled a **light filament/low-density filament**, consistent with sensor chain observations (Fig. 2). The steepening of isopycnals (Fig. 2c) matches downwelling, while the sensor chain's decreasing vertical filament extent coincides with drifter-indicated upwelling.

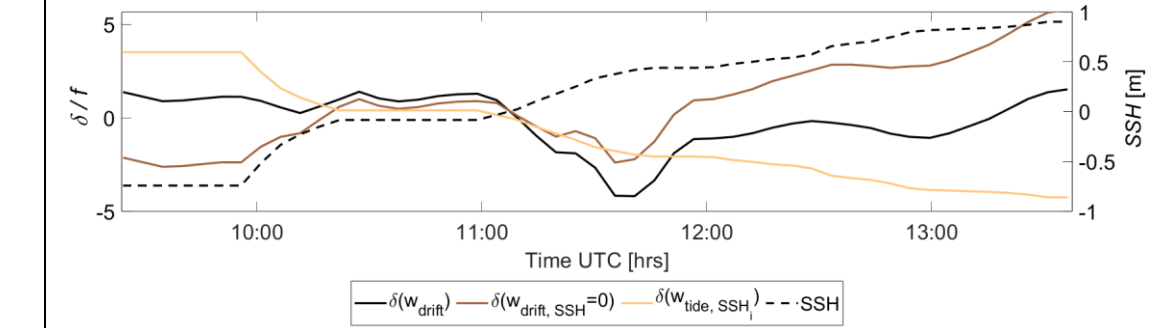


340 **Figure 3. Divergence and vertical velocity patterns observed during high tide period.** a) Trajectories of the centroids from drifter triplets over latitude and longitude colored according to time on August 5th. The map background displays the corresponding isohales in $\text{g} \cdot \text{kg}^{-1}$ (CMEMS, 2024; gray solid lines) as mean over the displayed drifter period. b) Normalized near-surface divergence and c) vertical velocity in $\text{m} \cdot \text{d}^{-1}$ for the time sections of drifter triplets in a) colored according to northern (magenta) and southern (grey) drifter triplet clusters. Black outlines highlight the sampling of the filament.

345 The southern cluster showed weaker divergence, generally fluctuating between $\pm 2f$. At the filament location, these centroids did not display the diffraction seen in the northern cluster and remained on the 29.8 g kg^{-1} isohaline during peak tidal flow, whereas the northern cluster crossed diapycnally by $\sim -0.5 \text{ g kg}^{-1}$. Outside the filament, w exhibited an overall up- to downwelling trend for both clusters, reflecting decreasing tidal velocities (Fig. 3b). In regions of filament-induced vertical motion, tides either mediated or amplified w . For example, during the first convergence zone, filamentary downwelling was partly offset by tide-induced upwelling, while in the second convergence period, weaker tidal flow enhanced downwelling.

350 These results show that the light filament's evolution was embedded within and dynamically coupled to tidal currents. Sharp discontinuities observed outside the filament ($\sim 12 \text{ h}$) likely resulted from a secondary crossing of strong density gradients.

355 The contribution of tidal modulation to divergence is shown in a simplified model (spatially averaged means of divergence from drifter clusters) of the overall observed divergence, local filament divergence and tidal divergence (Fig. 4). After removing the local filament divergence $\delta(w_{drift,SSH} = 0)$, where no tidal displacement was incorporated, from the overall divergence $\delta(w_{drift})$, the remaining tide-induced divergence $\delta(w_{tide,SSH_i})$ indicates a reverse relation to the tidal phase of the high water. At early flood period ($\sim 11:30$) divergence is added to the system, whereas at late flood period, when the tidal current decelerates, convergence is added. For the local filament divergence dynamics this may cause an offset up to $\pm 3f$. Nevertheless, the functionality of this model is limited to the water surface and the resolution of the SSH data and needs further improvement to increase the quality of estimating the tide-induced divergence contribution.

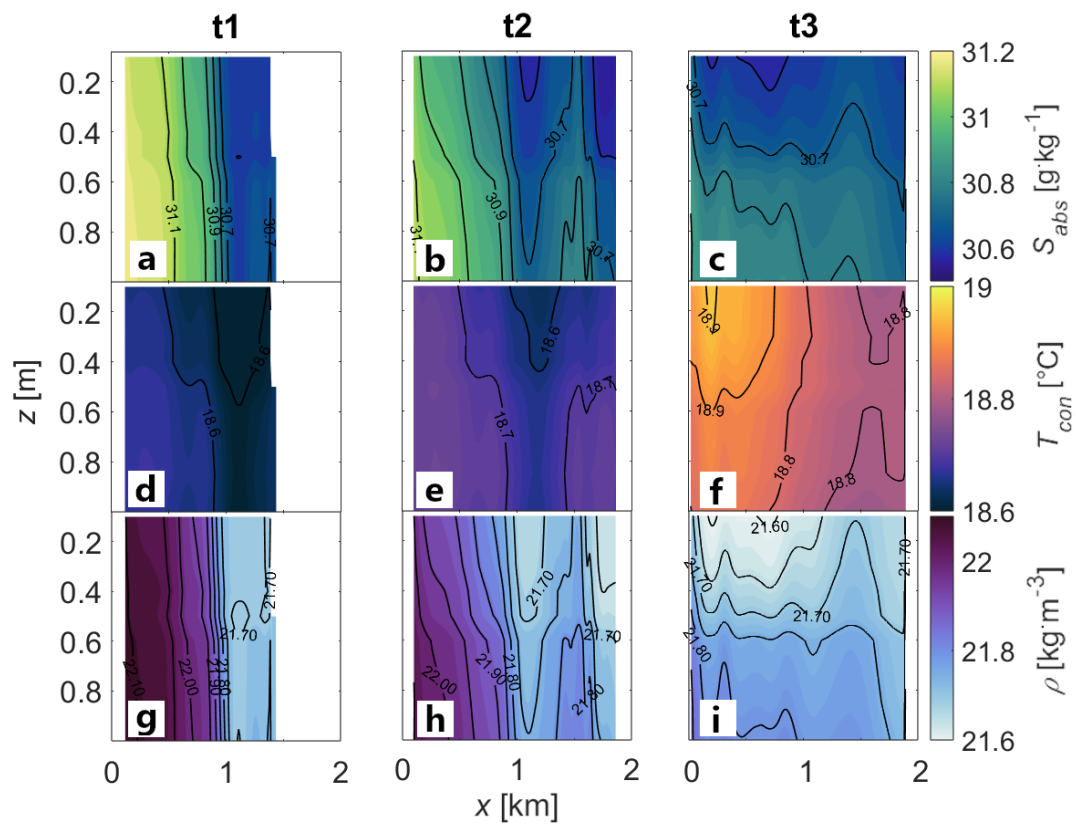


365 Figure 4. Time series of spatially-averaged divergence normalized by f calculated from drifter triplets incorporating tidal displacement (black bold line) and excluding tidal displacement ($w_0(z = 0)$; brown line). Subtracting both divergence modes results in divergence budgeted resulting only from tidal displacement (yellow line). All modes are displayed in relation to the tidal phase indicated by SSH (black dotted line).

3.3 Filament structure and evolution of isopycnals in the overlying first meter

370 While with the data analyzed in sections 3.1 and 3.2 identified the low-density filament during the high tide period, data by the ASV (sections 3.3 and 3.4) address the filament observed during low tide. During this period~~During the ebb period~~, three phases were recognized in the evolution of the ~~light filament~~low-density filament in the overlying first meter of the NSL (Fig. 54). Panels a, d, g show phase I, where isopycnals were vertically aligned and density varied by about 0.4 kg m^{-3} over less than 0.5 km. Although data are only available for $x < 1.5 \text{ km}$, profiles at t1 reveal a fresh (30.6 g kg^{-1}) and cold ($18.6 \text{ }^\circ\text{C}$) filament core at $1.0 \text{ km} < x < 1.5 \text{ km}$, contrasting with surrounding water masses along the transect. Density gradients were due to 10 times stronger influence of salinity ($\Delta\rho(S) \approx 0.54 \text{ kg m}^{-3}$) than temperature ($\Delta\rho(T) \approx 0.04 \text{ kg m}^{-3}$) (not shown), identifying the low-density filament as salinity-driven due to high freshwater contrasts.~~This indicates the initial formation of a light water mass intrusion on the light side of the TME.~~

375



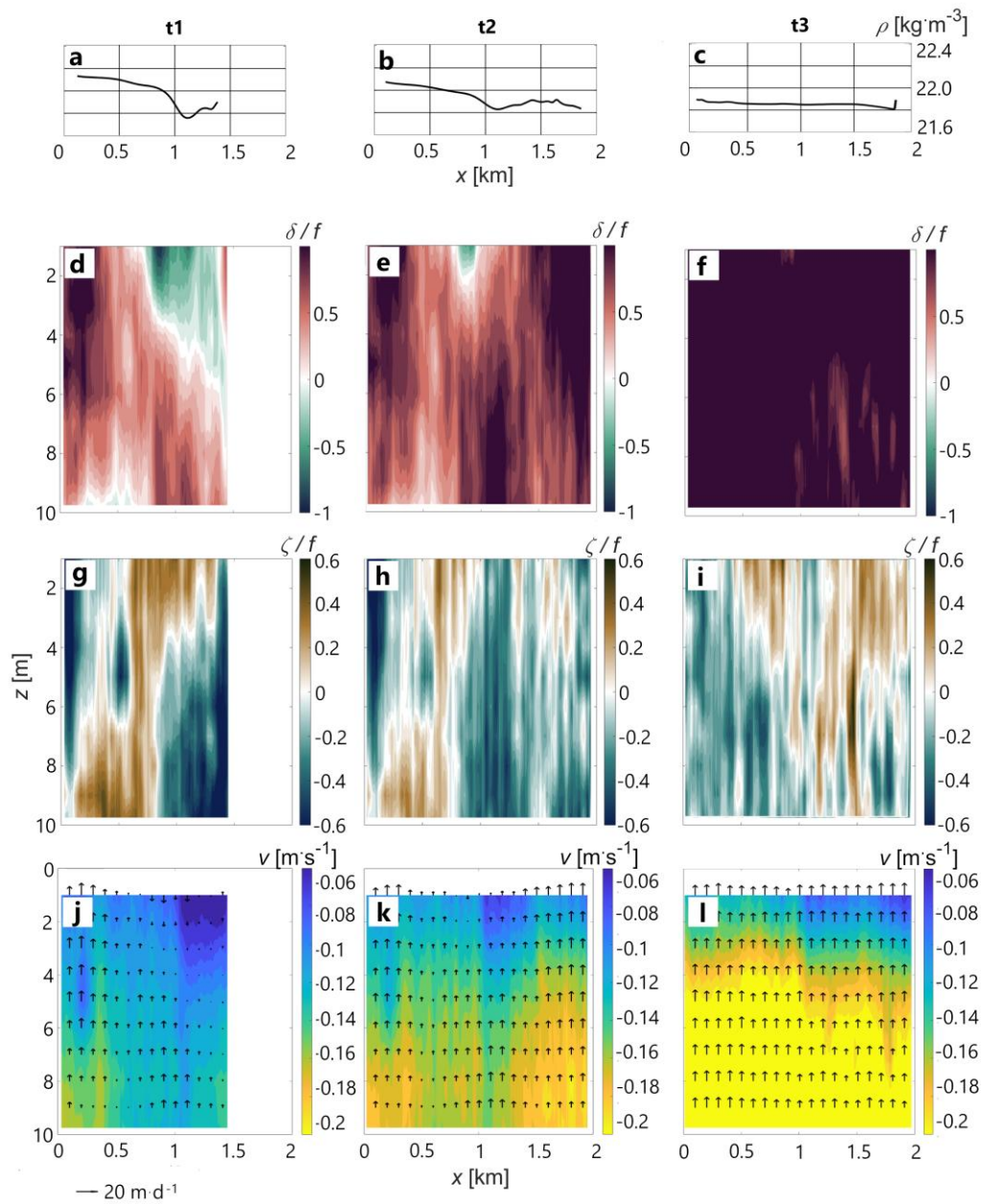
380 **Figure 45.** CTD data from the ASV displayed as contour section over depth across the filament at t1 = 07:23 am, t2 = 07:40 am and t3 = 08:30 am, each for of a-c) absolute salinity, d-f) conservative temperature and g-i) potential density in the upper NSL.

In phase II (t₂; Fig. 54b, e, h), isopycnals above 0.6 m began to flatten away from the filament axis, and the light core of the filament shifted into the upper layer above 0.6 m, with a slight intensification of about 0.1 kg m⁻³ (Fig. 54h). Below 0.6 m, no flattening occurred, but the temperature gradient decreased, with a minor reduction in salinity (Fig. 54b,e). This led to compression of the filament core, reducing its horizontal extent in this layer to roughly half of its initial length. Phase III (t₃; Fig. 4c, f, i) occurred less than one hour later. Isopycnals were now nearly horizontal, and the ~~light filament~~low-density filament core was distributed homogeneously in the upper 0.6 m (Fig. 54i). Salinity followed the density pattern, while temperature became horizontally stratified with a gradient of ~0.2 °C.

Throughout the observation period, the filament core salinity remained at 30.6 g kg⁻¹ (Fig. 54a-c), while the surrounding water mass decreased by ~0.4 g kg⁻¹. Temperature within the filament increased by ~0.3 °C, compared to ~0.1 °C in the surrounding water (Fig. 45d-f). Salinity primarily controlled density, which decreased by ~0.1 kg m⁻³ within the filament and ~0.3 kg m⁻³ in the surrounding water (Fig. 54g-i). The observed evolution of the ~~light filament~~low-density filament exhibits characteristics reminiscent of filamentogenesis, including upward displacement of the light core and lateral compression. Unlike classical cases documented in the literature (e.g.; McWilliams et al., 2015; Chrysagi et al., 2021; Jakes et al., 2023), these dynamics are driven primarily by salinity gradients rather than temperature gradients, reflecting the strong influence of freshwater input and tidal modulation in the southern North Sea. While ASC patterns are not yet analyzed, these observations suggest the filament is undergoing a process analogous to filamentogenesis, to be further confirmed with ADCP-derived velocity fields in the following section. Notably, the upward displacement of the filament core is consistently observed across all datasets: the sensor chain covering the NSL below 1 m, the drifter trajectories, and the ASV CTD measurements in the upper meter, reinforcing the robustness of this evolution.

3.4 ASC patterns and evolution of divergence, vorticity and vertical velocity in the near-surface layer

During phase I of the filament evolution in the NSL, divergence occurred around the Coriolis frequency f , with a significant convergence area between $x = 0.5$ km and $x = 1.5$ km (Fig. 65d). Over depth, the convergence core extended from 4 m at $x \approx 1$ km down to 8 m at $x = 1.5$ km. Dense water sank along the TMF density gradient (Fig. 65a) at ~15 m d⁻¹ (Fig. 56j), accumulating beneath lighter water (Fig. D1). This downwelling also dragged light water downward at about half the magnitude of w . Below the convergence zone, divergence developed alongside anticyclonic vorticity for $x > 1$ km and cyclonic vorticity for $x < 1$ km, both within the Rossby radius (Fig. 65g; Thomas et al., 2008), producing uplift of the filament flanks at ~12 m d⁻¹. CTD profiles (Fig. D1) confirmed dense bottom water being advected upward into shallower layers by divergence flow. These ASC signals correspond to a reversed pattern of ~~light filament~~low-density filamentogenesis, i.e. filamentolysis, characterized by downwelling in the core and uplift on the flanks.



415 **Figure 56. Sections of low-density filament kinematics.** a-c) Density profile over distance from ASV CTD data at $z=100$ cm for $t_1 = 07:23$ am, $t_2 = 07:40$ am and $t_3 = 08:30$ am on August 5th in the NSL. Underlying panels show corresponding sections over depth of normalized d-f) δ , g-i) ζ and j-l) along-front velocity with overlying w (arrows) referenced to 20 m d^{-1}

420 In phase II, ~~the ASC signatures shifted.~~ As divergence increased, the convergence core contracted vertically by $\sim 2\text{-}3$ m and horizontally by ~ 0.25 km within 17 minutes (Fig. 56e). The steep density gradients relaxed through mixing, reducing downward motion (Fig. 65k), while CTD profiles showed flattening isopycnals at $z = 100$ cm. Anticyclonic divergence expanded toward the surface on the right boundary (Fig. 65e,h), driving upwelling up to 20 m d^{-1} (Fig. 65k) and exporting dense water laterally away from the ~~TMF axis~~ filament. Vertical shear in the along-front velocity (Fig. 6k) was additionally higher on the right side of the filament, potentially causing advection or enhanced stirring. The general increase in along-front velocity over throughout t1-t3 may be due to the late phase of low tide. There, the flood current already sets in in the bottom layer, while the ebb current still flows at the surface (Fig. E1). This tidal asymmetry develops due to the freshwater contrasts between the surface and lower layers, causing upwelling near the sea floor. On the left side, strong divergence and anticyclonic vorticity brought dense water upward into the convergence zone (Fig. 5h). Overall, phase II represented a transitional regime: the strong downwelling of phase I largely disappeared, but the complete boundary downwelling characteristic of filamentogenesis had not yet emerged. Instead, ASC signatures combined remnants of filamentolysis with early signs of filamentogenesis, suggesting that the main circulation had already shifted upward into the overlying first meter.

430

By phase III, the ASC patterns below 1 m revealed only the tails of the process. The density at $z = 100$ cm dropped by $\sim 0.3 \text{ kg m}^{-3}$ on the left side (Fig. 65c), consistent with vertical CTD profiles. During the final 40 minutes, the anticyclonic patch doubled in magnitude and extended through the full water column (Fig. 65i), while a cyclonic patch developed at $x < 1.5$ km, inducing upwelling toward the TMF axis. The stronger cyclonic upwelling displaced the convergence core at $x = 1$ km, replacing it with lateral advection of dense water toward the ~~high filament~~ low-density filament. Unlike in phase II, where ASC signals were mixed and transitional, phase III was marked by intensified divergence and upwelling, pointing to the fact that true filamentogenesis had now strengthened above 1 m. This interpretation is supported by the restratification of isopycnals at 0.6 m in the ASV CTD data (Fig. 54) and the drifter observations at 0.5 m, which captured the surface expression of filamentogenesis that the ADCP could only detect indirectly.

435

440 Taken together, the ASC patterns evolved from reversed circulation in phase I (filamentolysis), through a transitional mixture in phase II, to enhanced filamentogenesis above 1 m in phase III, with only its residual upwelling detectable below. This sequence reflects the canonical circulation patterns of ~~high filament~~ low-density filamentogenesis (McWilliams et al., 2015; Jakes et al., 2023), but with the unique distinction that in the North Sea ~~TMF~~ tidal mixing front, salinity, rather than

temperature, dominated the gradients driving filament evolution. Furthermore, the observe patterns show an asymmetry, where the right side of the filament was prone to different local kinematics than the left side of it. Importantly, the ASC observations add a dynamic perspective to the restratification processes already identified in the sensor chain, drifter, and ASV CTD datasets, confirming that the filament's uplift was a coherent, cross-dataset signal in the upper water column.

4 Discussion

The synoptic-Lagrangian in situ observations in this study show a narrow, light filament/low-density filament that formed due to freshwater-driven buoyancy and was embedded in a TMF-tidal mixing front that showed a distinctive response to the tidal flow, and over the day heat transport, indicating the importance of surface filaments for the air-sea interface. Filaments store potential energy and act to capture the kinetic energy of waves, tides, and currents (Thomas et al., 2008), mainly when biofilms occur at convergence zones and the wave-dumping effect is visible (Wurl et al., 2016). The filament established in the lower and overlying first meter of the NSL (Fig. 2 and 54), features strong surface convergence guided by same-order divergence, suggesting the development of an ASC (Fig. 64; McWilliams et al., 2015) that may favor the exchange of gases, nutrients (from biofilms), heat and, energy between the ocean surface, deeper layers and the atmosphere. Taking this interaction potential as motivation, the goal of this section is to understand the evolution of filamentary structure and flow in a highly dynamic regime in the near-surface layer of the ocean.

460 *a. Evidence and structure of the light filament/low-density filament*

The observations provide robust evidence for the occurrence of a light filament/low-density filament embedded in a tidal mixing front-(TMF) in the southern North Sea. Signals of uplift, convergence, and buoyancy production were consistently detected across all independent datasets. The sensor chain captured the filament during flood as a sharp density contrast driven by freshwater contrasts and buoyancy signal relative to the surrounding waters. It also confirmed that the filament formed on the light side of the TMF-tidal mixing front, as isopycnal characteristics and stratification shifted markedly during the front crossing under the combined influence of southeasterly winds and the tidal ebb wave at 5 pm. Drifters independently captured the filament through trajectory diffraction and associated divergence-convergence patterns at its boundaries. ASV CTD transects during ebb revealed the filament as an even sharper horizontal density gradient within the uppermost meter, although the right filament border could not be fully resolved due to the transect length. ADCP profiles complemented these results by recording a full convergence signal across the filament, extending approximately 0.8 km horizontally and 4-8 m vertically. The repeated detection of the filament during both ebb and high tide underscores that it was a genuine TMF feature rather than a tidal current artifact. Furthermore, in all data sets an asymmetry in filament structure occurred, with the right border of the filament being eroded stronger than the left side over time.

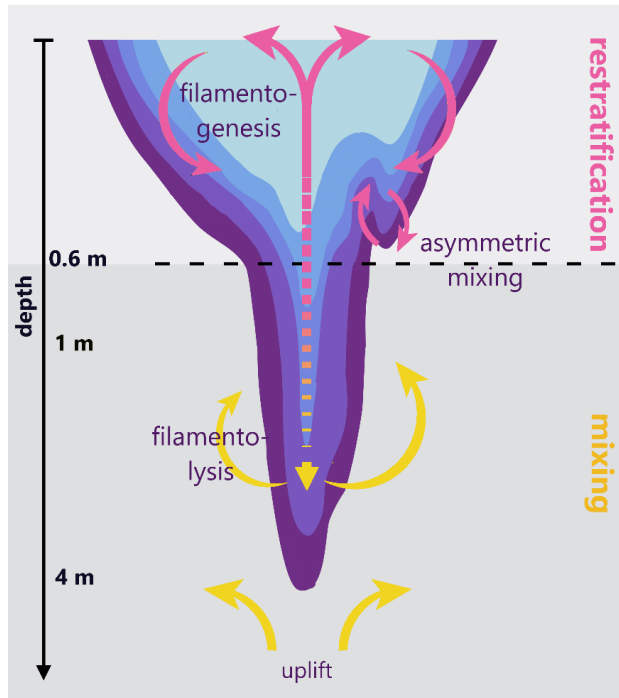
475 Unlike dense filaments, which tend to form recurrently and persist over longer periods (McWilliams, 2009; Chrysagi et al.,
2021; Garcia-Jove et al., 2022), ~~light filament~~low-density filaments are said to appear far more volatile. The observed low-
density filament depended highly on freshwater-driven buoyancy and tidal redistribution, which continuously reshape near-
surface density gradients. They are scarcer, ephemeral, and strongly sensitive to freshwater input and tidal redistribution,
~~which continuously reshape near surface density gradients.~~ Their buoyant positioning at the very top of the water column
480 likely ~~explains impact~~ this fragility, since atmospheric forcing and tidal stirring act directly on the gradients that sustain
them. Importantly, the gradients here were salinity-driven, in clear contrast to the temperature-driven dense filaments that
dominate open-ocean settings (Mahadevan & Tandon, 2006; McWilliams et al., 2015; Jakes et al., 2023). This salinity
control represents a unique pathway for filamentogenesis, potentially characteristic of shelf and estuarine systems such as the
North Sea.

485

b. ASC patterns in the overlying first meter and lower NSL

The ASV CTD and ADCP measurements together provide a coherent view of filament ASC patterns, revealing three distinct
phases that unfolded over the short span of only one hour. This rapid timescale ~~highlights may explain~~ the ~~transient~~
~~naturescarce observations~~ of ~~light filament~~low-density filaments and the inherent difficulty of capturing their dynamics in
490 the field. However, high-resolution multi-sensor and -platform measurements help observing these processes as shown in
this study.

In Phase I, the filament exhibited a sharp horizontal density gradient and a cone-like structure as Jakes et al. (2023)
schematized. Yet the associated ASC in the NSL > 1 m, however, showed rather a filamentolysis pattern with downwelling
495 occurring within the core and uplift at the flanks. Upwelling from the near-bottom was induced by tidal modulation (see
section c.) and along-front vertical velocity shear advecting density gradients differentially (Johnson et al., 2020). The
vertical shear arises from the already propagating flood current in the bottom layer, while the ebb current still persists at the
surface (Burchard and Badewien, 2015; Stanev et al. 2015) and might be fuelled a consequence of down-front wind in the
500 direction of the surface frontal jet, slowing down velocities in the upper and enhancing mixing in the lower NSL
(Mahadevan and Tandon, 2006; Thomas et al., 2008). This instability acted to erode the filament, setting the stage for
subsequent transitions in phases II and III.



505 | Figure 76. Schematic process of filamentolysis-induced filamentogenesis in the NSL. ASC associated with upper-NSL filamentogenesis (restratification) is colored pink, ASC associated with lower-NSL filamentolysis (mixing) is yellow.

510 | In Phase II (Fig. 76), downwelling in the lower NSL weakened due to the decrease in density gradient strength, while signals of upwelling and divergence intensified. This intensification, however, caused spatially asymmetric erosion, with earlier and stronger weakening on the eastern/right-hand side of the filament. This asymmetry coincides with evolving kinematic conditions, including a gradual reduction of convergent signatures in δ/f , increasingly patchy anticyclonic vorticity, and a broadening of the secondary circulation. In addition, across-front velocity sections show stronger near-surface across-filament flow and enhanced horizontal and vertical shear on the eastern side, suggesting locally intensified differential advection or lateral stirring, both vertically and horizontally.

515 | Above 0.6 m, early restratification established with flattening of isopycnals on both boundaries of the filament core, indicating downwelling, pointing toward potential filamentogenesis of a low-density filament in the upcoming 40 min. Early restratification established above 0.6 m with flattening of isopycnals on both boundaries of the filament core, indicating downwelling. The resulting ASC depicts the filamentogenesis of a light

520 ~~filament in the upcoming 40 min.~~ The loss of buoyancy in the lower layer, therefore, fueled buoyancy production in the upper NSL, resulting in a two-layer coupled filamentolysis-filamentogenesis process.

In Phase III, these signatures intensified further: divergence broadened, upwelling strengthened, so that below 1 m the filament completely vanished from the water column. In the upper 0.6 m, restratification is fully established.

525 ~~A snapshot of the filamentogenesis pattern indicated by isopycnals, hinting toward~~
~~pattern, characterized by~~ upwelling in the core and downwelling at the flanks, was only captured in the upper 1 m (drifters, ASV CTD). Below 1 m, ADCP observations alone were insufficient to resolve the full pattern, recording only the lower NSL filamentolysis. This highlights the importance of simultaneous, co-located ASV CTD and ADCP measurements for resolving the vertical structure of ASC in the NSL and for disentangling the coupling of submesoscale processes across layers.

530

c. Tidal modulation of filament formation and vertical velocities

The observed ASC patterns were strongly modulated by tides, which both enhanced and suppressed filamentary circulation depending on phase. Drifter data reveal that acceleration of the tidal flow induced divergence and upwelling, whereas deceleration toward low water produced convergence and downwelling. Due to the temporal offset between ASV and drifter
535 deployments, the time series of drifter data was too short to resolve the coupling of tides with the filament at ebb tide. However, together with the data from the sensor chain, the tidal modulation of the filament could be resolved during high tide.

540 Within the simplified tidal-modulation framework based on Copernicus SSH-derived divergence (section 3.2), decelerating ebb flow would generally be expected to enhance convergence and support downward motion within the filament. However, the observations do not clearly reflect this expected strengthening of convergence. One possible contributing factor may be a vertical phase structure in the tidal circulation, where flood flow already intrudes the lower water column while ebb current still propagate near the surface. In such a configuration, the expected convergent tendency may potentially weakened by upwelling caused by the underneath accelerating flood current or local filament upwelling. Constructive and destructive interference between tidal motions and filament-induced circulation may have further modulated vertical velocities, contributing to the observed reduction in filament coherence, as also reflected in the sensor chain signal (section 3.1). Overall, the filament appears to have evolved within a kinematically heterogeneous environment where evolving patchy anticyclonic vorticity and local shear structures likely modulated the background tidal convergence field. Given the simplified nature of the tidal-modulation estimate and the limited spatial resolution of the forcing fields, the relative contributions of tidal forcing, vertical phase structure, and local advection processes remain difficult to fully disentangle, but
545 together they provide a consistent qualitative framework for the observed asymmetric erosion.

550

~~Destructive interference of tidal upwelling suppressed downwelling, reducing the filament's tendency to filamentolysis. Conversely, constructive interference occurred when tidal upwelling coincided with filamentary upwelling, amplifying upward velocities. This coincides with the reduction of the filament in the sensor chain signal that resembled the evolution of the filament in the upper NSL, supposing a similar process as in section b. This feedback further explains the asymmetric responses of the filament's borders: the left flank remained comparatively stable, while the right flank eroded in the vertical at a rate of $25 \text{ m}\cdot\text{min}^{-1}$ and twice as fast as the left flank in the horizontal at a rate of $0.2 \text{ m}\cdot\text{min}^{-1}$ under the constructive interference of filament and tidal downwelling after the current of the high tide started to decelerate.~~

Quantitatively, divergence values at the observed TMF reached 1-4 times higher than those reported in the Alboran Sea (Rypina et al., 2021; Garcia-Jove, 2022; Esposito et al., 2023) or the Bay of Bengal (Essink et al., 2022). While these exaggerated magnitudes may partly reflect overestimation by the area-based drifter method due to rapid tidal deformation of drifter triplets, they nonetheless point to strong tide-filament interactions. The resulting vertical velocities reached up to $50 \text{ m}\cdot\text{d}^{-1}$ during divergence phases and down to $-40 \text{ m}\cdot\text{d}^{-1}$ during convergence phases. Comparisons between methods further highlight the tidal imprint, so that drifter-based estimates were roughly twice as large as ADCP-derived velocities, but converged to similar magnitudes once tidal displacement at the surface is removed from the drifter calculations.

d. Implications for surface exchange and heat uptake

Once filamentogenesis was established in the upper meter, the system became more efficient at absorbing heat, with uptake doubling despite only weak net temperature changes. This enhanced capacity highlights the importance of ~~light filament~~low-density filaments as effective, short-lived hotspots of exchange at the ocean-atmosphere interface. Tidal modulation, salinity redistribution and rapid phase transitions may make them mediators of vertical exchange. While dense filaments dominate in the open ocean, ~~light filament~~low-density filaments may represent a likely important, yet less frequent, pathway for near-surface fluxes in shelf and estuarine seas.

5 Conclusion and Outlook

The study provides ~~synoptic multi-dataset~~ observations of a ~~salinity driven light filament~~low-density filament on the submesoscale [$O(0.1-10 \text{ m})$] ~~driven by freshwater-driven buoyancy~~ embedded and modulated within a tidal mixing front. By combining complementary datasets from sensor chains, drifters, ASV CTD transects, and ADCP profiles, a coherent sequence of filament evolution and associated ageostrophic secondary circulation (ASC) was identified that unfolded on timescales of approximately one hour. The three observed phases highlight the coexistence of filamentolysis in the deeper near-surface layer and filamentogenesis confined to the upper meter, revealing a tightly coupled, layer-dependent response that could only be captured through multi-instrument, high-resolution observations.

585 Unlike dense, temperature-driven filaments previously described in the open ocean, the ~~light filament~~low-density filament observed here associated with strong freshwater-driven buoyancy contrasts, highlighting a distinct estuarine pathway to filament formation. The observations further suggest that tidal modulation strongly influenced the filament structure and surface divergence patterns, with different tidal phases associated with amplification or weakening of the frontal signal. This tidal influence may also contribute to local filament processes such as the asymmetric erosion of filament flanks and the transition from strong lateral buoyancy gradients toward restratification. ~~was volatile, short-lived, and strongly modulated by tidal forcing. Its dynamics were further shaped by the redistribution of freshwater-derived salinity gradients, underscoring a unique estuarine pathway to filamentogenesis. The interplay of tidal currents with filamentary ASC produced constructive and destructive interference, explaining both the asymmetric erosion of filament flanks and the transition from strong lateral buoyancy gradients to restratification.~~

590 Restratification during filamentogenesis coincided with enhanced surface warming, suggesting a potential link between submesoscale circulation and upper-ocean heat storage. Our observations further indicate that freshwater-driven buoyancy contrasts play a central role in filament formation, while tidal modulation can amplify or weaken the surface divergence signal depending on tidal phase. However, the use of sea surface height for the estimation of tidal modulation of the divergence budget only provides a simplified model that is restricted to the surface. Since dense North Sea water and less dense water mixed with freshwater originating from rivers such as Elbe and Weser create a vertical tidal phase shift, it is crucial to also incorporate tidal modulation in the deeper layers. Further, more synoptic spatial and temporal assessments are necessary to resolve the background and tidal flow accompanying the filament. These results thus are a first approach in coupling freshwater-driven buoyancy and tidal impact on a low-density filament that may contribute to vertical exchange and air-sea coupling in the ocean. Restratification during filamentogenesis substantially enhanced the upper layer's capacity to store heat, linking submesoscale circulation directly to surface energy budgets. In this way, the dynamic processes like tidal modulation, atmospheric forcing, and salinity control that make light filaments scarce and prone to fast decay also make them important for vertical exchange and air-sea coupling. More broadly, resolving the transient dynamics of buoyancy-driven filaments and their tidal modulation may improve our understanding of upper-ocean stratification and regional climate feedbacks. ~~More broadly, resolving the short-lived but impactful dynamics of light filaments is essential for improving climate models. Their ability to mediate rapid exchanges of heat, gases, and momentum at the air-sea interface suggests that submesoscale processes may play a significant role in shaping upper-ocean stratification and regional climate feedbacks.~~

605
610
615 Taken together, the results expand the current paradigm of filament dynamics by demonstrating a salinity-driven mechanism for coupled ~~light filament~~low-density filamentogenesis and -lysis in shelf seas. Future work should quantify the frequency of such features in estuarine and coastal systems and assess their role in larger-scale balances of heat, gas exchange, and energy. To advance this, improved synoptic measurement strategies are needed, featuring congruent CTD and ADCP

deployments that allow filamentary structure and ASC to be described more quantitatively, for instance, through frontal tendency calculations.

Appendices

620 Appendix A

Since horizontal divergence is used to diagnose vertical motion, the vertical velocity in the water column can be determined.

Restructuring the continuity equation $\frac{\partial u}{\partial x} + \frac{\partial v}{\partial y} + \frac{\partial w}{\partial z} = 0$ results in

$$\begin{aligned} \Delta w &= - \int_{-z}^{z^0} \left(\frac{du}{dx} + \frac{dv}{dy} \right) dz & (A1) \\ \leftrightarrow w(z_i) - w(z_{i-1}) &= \int_{z_i}^{z_{i-1}} \frac{du}{dx} dz \\ &= \left[\left(\frac{du}{dx} + \frac{dv}{dy} \right) z \right]_{z_i}^{z_{i-1}} \\ &= \left(\frac{du}{dx} + \frac{dv}{dy} \right)_{z_{i-1}} z_{i-1} - \left(\frac{du}{dx} + \frac{dv}{dy} \right)_{z_i} z_i \\ &= \left(\frac{du}{dx} + \frac{dv}{dy} \right) (z_{i-1} - z_i) \\ w(z_i) &= w(z_{i-1}) + \left(\frac{du}{dx} + \frac{dv}{dy} \right) \Delta z, \end{aligned}$$

630 where $w(z_i)$ is the vertical velocity in the target depth z_i , $w(z_{i-1})$ is the vertical velocity in the previous depth z_{i-1} and Δz is the difference between neighboring depths. For $w(z_{i-1})$ of the drifters, the SSH (Fig. A3) is obtained from model data (CMEMS, 2024) to emulate the vertical velocity that arrives from the tidal wave

$$635 \quad w(z_{i-1}) = \frac{1}{n} \sum_{k=1}^n \text{ssh}_k \cdot \frac{1}{\Delta t}, \quad (A2)$$

where ssh_k is the tidal amplitude and $\Delta t = 1 \text{ h}$ is the temporal resolution of the model data. Thus, $w(z_{i-1})$ will be applied to (5) as hourly mean with a standard deviation of $\pm 0.3 \text{ m}$ resulting in an error $\Delta w(z_{i-1}) \approx 7 \text{ m} \cdot \text{day}^{-1}$.

640

Formatiert: Englisch (USA)

Formatiert: Englisch (USA)

Formatiert: Englisch (USA)

Formatiert: Englisch (USA)

Formatiert: Englisch (USA)

Formatiert: Englisch (USA)

Formatiert: Englisch (USA)

Formatiert: Englisch (USA)

Formatiert: Englisch (USA)

Formatiert: Englisch (USA)

Formatiert: Englisch (USA)

Formatiert: Englisch (USA)

Formatiert: Englisch (USA)

Formatiert: Englisch (USA)

Formatiert: Englisch (USA)

Formatiert: Englisch (USA)

Formatiert: Englisch (USA)

Formatiert: Englisch (USA)

Formatiert: Englisch (USA)

Formatiert: Englisch (USA)

Formatiert: Englisch (USA)

Formatiert: Englisch (USA)

Formatiert: Englisch (USA)

Formatiert: Englisch (USA)

Formatiert: Englisch (USA)

Formatiert: Englisch (USA)

Formatiert: Englisch (USA)

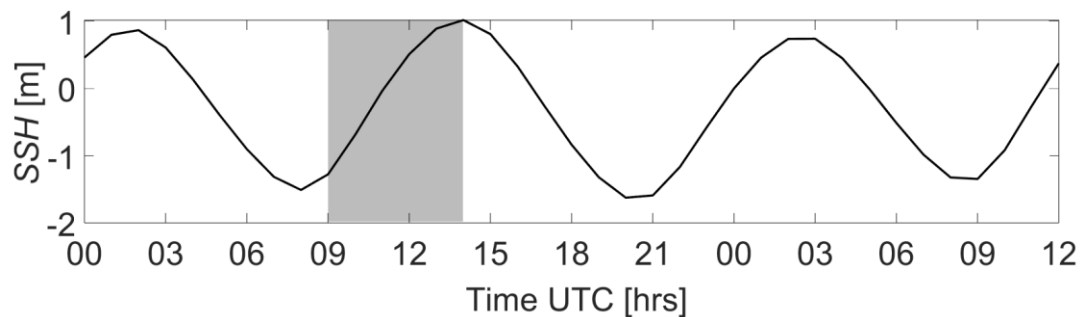


Figure A3. Hourly mean SSH obtained from model data (CMEMS, 2024) for the drifter deployments. The observation time of the filament is shaded in grey.

645

Appendix B

650

The correlation of model SSS (CMEMS, 2024) with salinity recorded by a Ferrybox flow-through system is shown in Fig. S1. For each spatial bin of the model data at a time step, Ferrybox salinity data is averaged within that bin and at that specific time. Proceeding like this for the three consecutive days (August 4th to 6th), the resulting data points are plotted for standard deviation, time, latitude and longitude. Applying a linear regression to the correlation, a R^2 of 0.705 can be achieved. The standard deviation throughout the correlation data lies on average below 0.05 g kg^{-1} and reaches only in a few exceptions $0.1\text{-}0.15 \text{ g kg}^{-1}$ that are not covered by the regression. Regarding the temporal distribution, especially the slack water times from late August 4th and whole 5th fall out of the regression. In terms of latitude, those outliers are mostly pronounced in higher latitudes ($> 54.2^\circ\text{N}$) and for longitude in eastward values ($> 8.1^\circ\text{E}$). The model data, thus, underestimates the salinity in the eastern, more coastal areas, probably assuming a higher freshwater input and hence a lower salinity than was obtained by the Ferrybox. In particular during low water, when the ebb current exports the more saline water seawards, the model predicts a lower reduced salinity. Compared to this, in more western areas, in between the slack water times, the estimation of the model is much better.

660

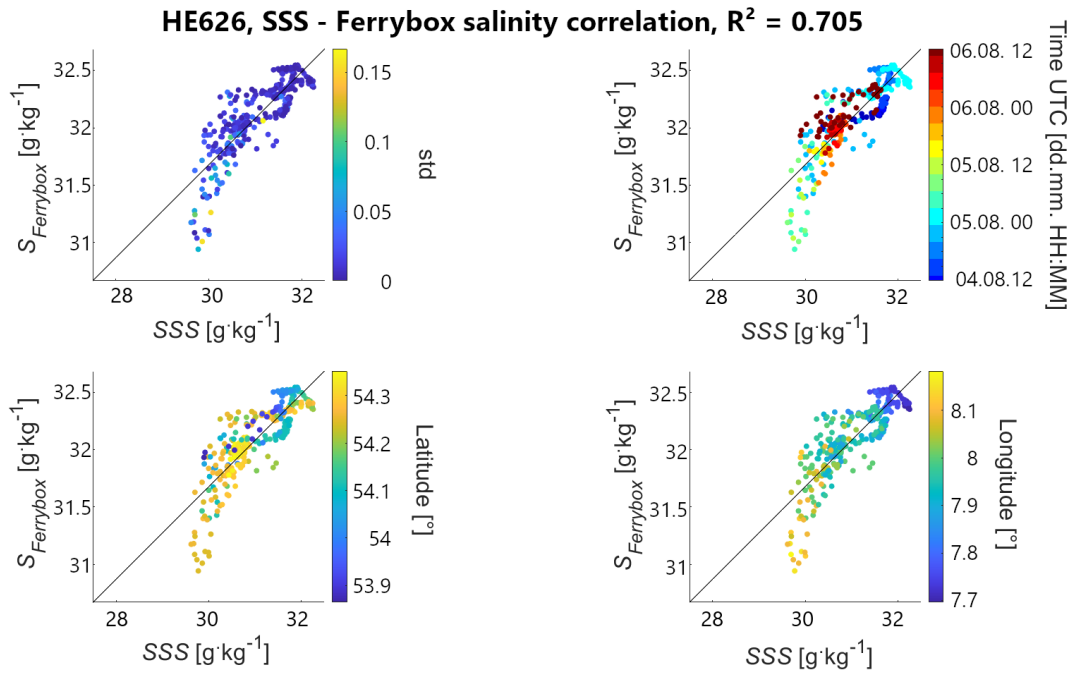
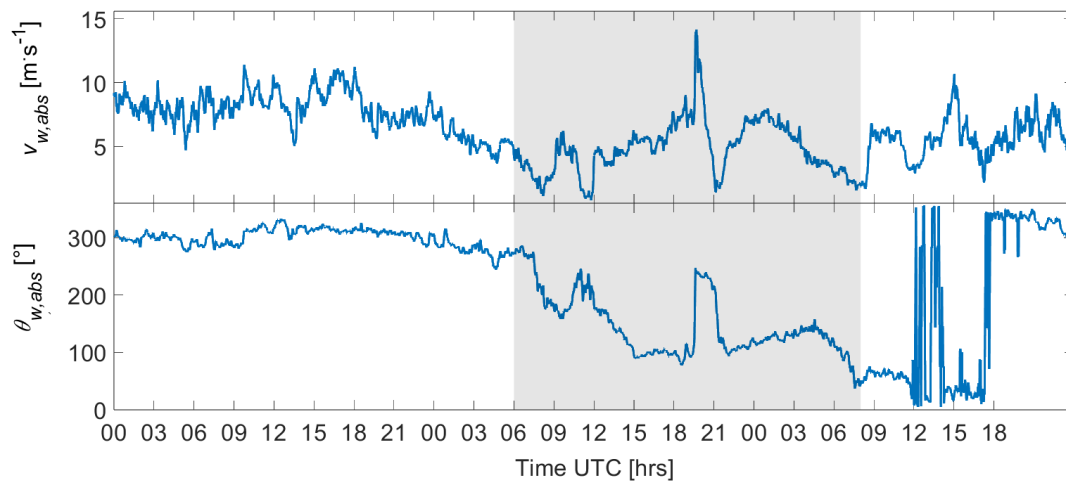


Figure B1. Correlation of SSS from model data (CMEMS, 2024) and Ferrybox salinity regarding (a) salinity standard deviation, (b) time (UTC), (c) latitude and (d) longitude. The linear regression model results in a correlation of $R^2 \approx 0.71$.

665

Appendix C



670

Figure C1. (top) Absolute wind speed $v_{w,abs}$ and (bottom) wind direction at 10 m $\theta_{w,abs}$ during the survey obtained from the weather station on RV Heincke. The grey shaded area highlights the period of the filament measurements.

Appendix D

675

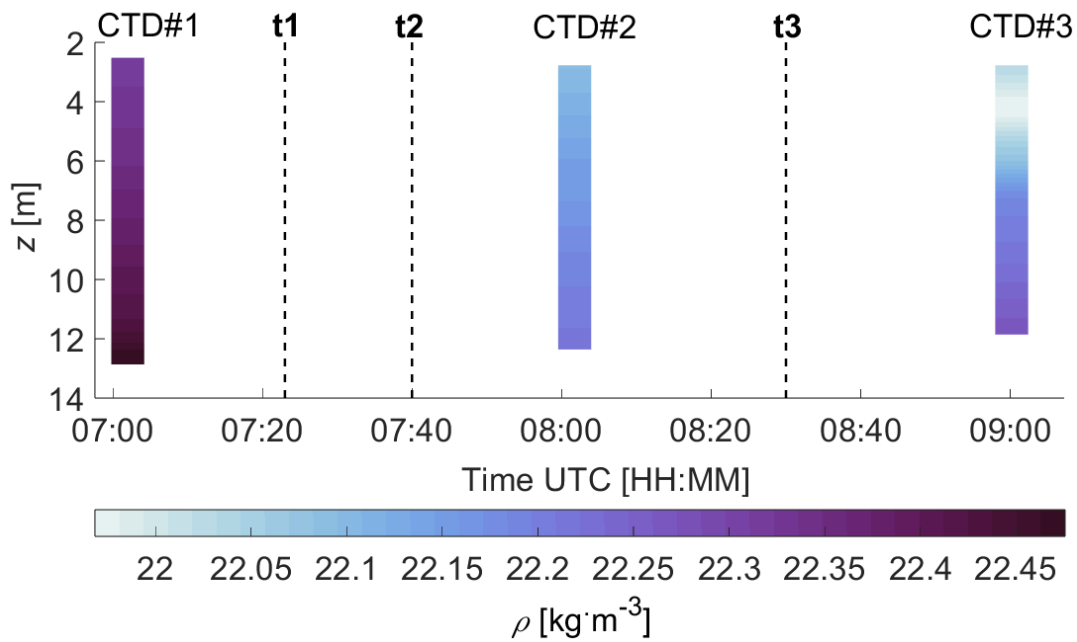


Figure D1. Vertical profiles of density from ship CTD during the observation period. Sections $t1-3$ from the filament analysis of the ASV data (sections 3.3 and 3.4) are marked as vertical dashed lines.

680

Appendix E

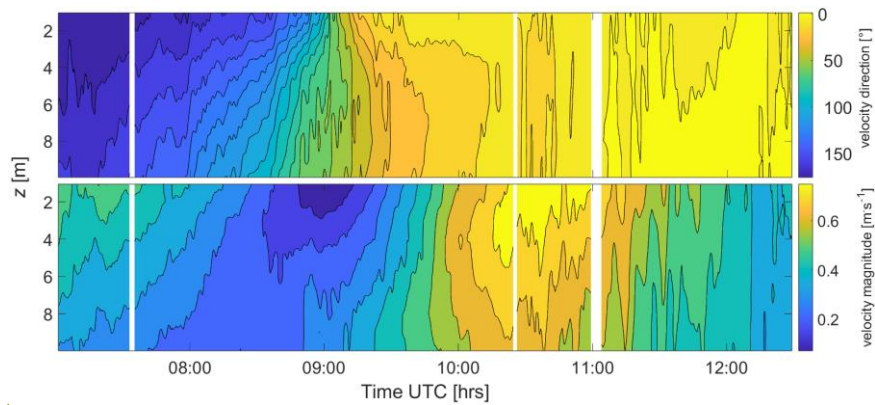


Figure E1. Contour of velocity magnitude and direction for August 5th over time and depth.

Formatiert: Schriftart: Fett

685 **Author contribution**

690 MA took the lead in writing the manuscript, conducting field measurements, processing and analysing data, and designing the figures. JM, LG and OW conducted field observations and data recording. OW and LJ processed the ASC CTD data. JM took the lead in supervising the work on the manuscript by streamlining the main concept and developing datasets and figures together with MA. THB supervised the project. All authors contributed to revising the manuscript by commenting on the manuscript and discussing the main concept and results of the study.

Formatiert: Schriftartfarbe:
Automatisch

Competing Interests

The authors state that they have no conflict of interest.

Acknowledgments

695 The authors would like to thank the captain and crew of RV Heincke and all the participants onboard for their support in collecting this dataset.

Financial Support

700 Financial support was received by the project “Sailing Intelligent Micro Drifter Swarms (Saimidris)” (grant no. VWZN3685) and “The North Sea from space: Using explainable artificial intelligence to improve satellite observations of climate change (North-SatX)” (grant no. VWZN3680). The study was conducted using resources of the “Biogeochemical processes and Air–sea exchange in the Sea-Surface microlayer (BASS)” framework (DFG; grant no. 451574234).

Data Availability Statement

705 Remotely sensed sea surface salinity, derived from model data, are available from the Copernicus Marine Environment Monitoring Service (CMEMS) at the following link <https://doi.org/10.48670/moi-00054>. CTD profile data (<https://doi.org/10.1594/PANGAEA.963643>), ASV-mounted ADCP data (<https://doi.org/10.1594/PANGAEA.973117>) and ASV CTD data (<https://doi.pangaea.de/10.1594/PANGAEA.972989>; in review) are published at Pangaea. Data from the sensor chain and the drifters are still in preparation and will be published on PANGAEA as soon as post-processing is completed. Raw data is available on request. Matlab-Code for computation and visualization of data is available on request.
710 ~~Remotely sensed sea surface salinity, derived from model data, are available from the Copernicus Marine Environment Monitoring Service (CMEMS) at the following link <https://doi.org/10.48670/moi-00054>. CTD profile data~~

~~(<https://doi.org/10.1594/PANGAEA.963643>), ASV-mounted ADCP data (<https://doi.org/10.1594/PANGAEA.973117>) and ASV-CTD data (<https://doi.pangaea.de/10.1594/PANGAEA.972989>; in review) are published at Pangaea.~~

References

715 [Albinus, M.; Deyle, L.; Gassen, L.; Herold, J.-M.; Meyerjürgens, J.; Wurl, O.; Badewien, T. H.: ADCP current measurements \(600 kHz\) from autonomous surface vehicle on 05.08.2023 during RV HEINCKE cruise HE626 \[dataset\]. PANGAEA, 10.1594/PANGAEA.973117, 2024.](#)

720 [Archer, M., Schaeffer, A., Keating, S., Roughan, M., Holmes, R., & Siegelman, L. Observations of submesoscale variability and frontal subduction within the mesoscale eddy field of the Tasman Sea. *Journal of Physical Oceanography*, 50\(5\), 1509-1529. 10.1175/JPO-D-19-0131.1, 2020.](#)

[Atlantic - European North West Shelf - Ocean Physics Analysis and Forecast. E.U. Copernicus Marine Service Information \(CMEMS\). Marine Data Store \(MDS\). 10.48670/moi-00054 \(Accessed on 06-Jan-2024\), 2024.](#)

725 [Ayim, S. M.; Bibi, R.; Cortés, E.; Gassen, L.; Jaeger, L.; Lehnert, C.; Ribas-Ribas, M.; Wurl, O.: High-resolution measurements of essential climate variables in the North Sea from the autonomous surface vehicle HALOBATES during RV Heincke cruise HE626 \[dataset\]. PANGAEA, 10.1594/PANGAEA.972989 \(dataset in review\).](#)

730 [Berta, M., Griffa, A., Magaldi, M. G., Özgökmen, T. M., Poje, A. C., Haza, A. C., & Olascoaga, M. J. Improved surface velocity and trajectory estimates in the Gulf of Mexico from blended satellite altimetry and drifter data. *Journal of Atmospheric and Oceanic Technology*, 32\(10\), 1880-1901, 10.1175/JTECH-D-14-00226.1, 2015.](#)

735 [Berta, M., Griffa, A., Özgökmen, T. M., & Poje, A. C. Submesoscale evolution of surface drifter triads in the Gulf of Mexico. *Geophysical Research Letters*, 43\(22\), 11-751. 10.1002/2016GL070357, 2016.](#)

[Burchard, H., & Badewien, T. H. Thermohaline residual circulation of the Wadden Sea. *Ocean Dynamics*, 65\(12\), 1717-1730. 10.1007/s10236-015-0895-x, 2015.](#)

740 [Chegini, F., Holtermann, P., Kerimoglu, O., Becker, M., Kreis, M., Klingbeil, K., ... & Burchard, H. Processes of stratification and destratification during an extreme river discharge event in the German Bight ROFI. *Journal of Geophysical Research: Oceans*, 125\(8\), e2019JC015987, 10.1029/2019JC015987, 2020.](#)

745 [Chrysagi, E., Umlauf, L., Holtermann, P., Klingbeil, K., & Burchard, H. High-resolution simulations of submesoscale processes in the Baltic Sea: The role of storm events. *Journal of Geophysical Research: Oceans*, 126\(3\), e2020JC016411, 10.1029/2020JC016411, 2021.](#)

750 [Deyle, L., Badewien, T. H., Wurl, O., & Meyerjürgens, J. Lagrangian surface drifter observations in the North Sea: an overview of high-resolution tidal dynamics and surface currents. *Earth System Science Data*, 16\(4\), 2099-2112, 10.5194/essd-16-2099-2024, 2024.](#)

755 [Drinkwater, K. F., & Loder, J. W. Near-surface horizontal convergence and dispersion near the tidal-mixing front on Northeastern Georges Bank. *Deep Sea Research Part II: Topical Studies in Oceanography*, 48\(1-3\), 311-339, 10.1016/S0967-0645\(00\)00084-9, 2001.](#)

760 [European North West Shelf/Iberia Biscay Irish Seas – High Resolution ODYSSEA L4 Sea Surface Temperature Analysis. E.U. Copernicus Marine Service Information \(CMEMS\). Marine Data Store \(MDS\). 10.48670/moi-00152. \(Accessed on 05-Aug-2023\), 2023.](#)

765 [Esposito, G., Donnet, S., Berta, M., Shcherbina, A. Y., Freilich, M., Centurioni, L., ... & Griffa, A. Inertial Oscillations and Frontal Processes in an Alboran Sea Jet: Effects on Divergence and Vertical Transport. *Journal of Geophysical Research: Oceans*, 128\(3\), e2022JC019004, 10.1029/2022JC019004, 2023.](#)

770 [Essink, S., Hormann, V., Centurioni, L. R., & Mahadevan, A. On characterizing ocean kinematics from surface drifters. *Journal of Atmospheric and Oceanic Technology*, 39\(8\), 1183-1198, 10.1175/JTECH-D-21-0068.1, 2022.](#)

775 [Garcia-Jove, M., Mourre, B., Zarokanellos, N. D., Lermusiaux, P. F., Rudnick, D. L., & Tintoré, J. Frontal dynamics in the Alboran Sea: 2. Processes for vertical velocities development. *Journal of Geophysical Research: Oceans*, 127\(3\), e2021JC017428, 10.1029/2021JC017428, 2022.](#)

770 [Gassen, L., Badewien, T. H., Ewald, J., Ribas-Ribas, M., & Wurl, O. Temperature and salinity anomalies in the sea surface microlayer of the South Pacific during precipitation events. *Journal of Geophysical Research: Oceans*, 128\(6\), e2023JC019638, 10.1029/2023JC019638, 2023.](#)

775 [Goßmann, I., Meyerjürgens, J., Albinus, M., Achnert, C., Robinson, B. T., Held, A., ... & Wurl, O. What influences the distribution of microplastics in the marine environment? An interdisciplinary study reveals key factors driving microplastic in the North Sea. *Science of The Total Environment*, 964, 178589, 10.1016/j.scitotenv.2025.178589, 2025.](#)

780 [Hill, A. E., James, I. D., Linden, P. F., Matthews, J. P., Prandle, D., Simpson, J. H., ... & Bowers, D. G. Dynamics of tidal mixing fronts in the North Sea. Philosophical Transactions of the Royal Society of London. Series A: Physical and Engineering Sciences, 343\(1669\), 431-446, 10.1098/rsta.1993.0057, 1993.](#)

[Holt, J., & Umlauf, L. Modelling the tidal mixing fronts and seasonal stratification of the Northwest European Continental shelf. Continental Shelf Research, 28\(7\), 887-903, 10.1016/j.csr.2008.01.012, 2008.](#)

785 [Huntley, H. S., Berta, M., Esposito, G., Griffa, A., Mourre, B., & Centurioni, L. Conditions for Reliable Divergence Estimates from Drifter Triplets. Journal of Atmospheric and Oceanic Technology, 39\(10\), 1499-1523, 10.1175/JTECH-D-21-0161.1, 2022.](#)

790 [Jakes, M. I., Phillips, H. E., Foppert, A., Cyriac, A., Bindoff, N. L., Rintoul, S. R., & Thompson, A. F. Observational Evidence of Cold Filamentary Intensification in an Energetic Meander of the Antarctic Circumpolar Current. Journal of Physical Oceanography, 54\(3\), 717-740, 10.1175/JPO-D-23-0085.1, 2024.](#)

795 [Johnson, L., Lee, C. M., D'Asaro, E. A., Thomas, L., & Shcherbina, A. Restratification at a California current upwelling front. Part I: Observations. Journal of Physical Oceanography, 50\(5\), 1455-1472, 10.1175/JPO-D-19-0203.1, 2020.](#)

[Kawai, H. Scale dependence of divergence and vorticity of near-surface flows in the sea: Part I. Measurements and calculations of area-averaged divergence and vorticity. Journal of the Oceanographical Society of Japan, 41\(3\), 157-166, 10.1007/BF02111115, 1985 .](#)

800 [Lapeyre, G., & Klein, P. Impact of the small-scale elongated filaments on the oceanic vertical pump. Journal of marine research, 64\(6\), 835-851, 10.1357/002224006779698369, 2006.](#)

805 [Mahadevan, A., & Tandon, A. An analysis of mechanisms for submesoscale vertical motion at ocean fronts. Ocean Modelling, 14\(3-4\), 241-256, 10.1016/j.ocemod.2006.05.006, 2006.](#)

[McWilliams, J. C., Colas, F., & Molemaker, M. J. Cold filamentary intensification and oceanic surface convergence lines. Geophysical research letters, 36\(18\), 10.1029/2009GL039402 , 2009.](#)

810 [McWilliams, J. C., Gula, J., Molemaker, M. J., Renault, L., & Shchepetkin, A. F. Filament frontogenesis by boundary layer turbulence. Journal of Physical Oceanography, 45\(8\), 1988-2005, 10.1175/JPO-D-14-0211.1, 2015.](#)

- 815 [McWilliams, J. C. Submesoscale currents in the ocean. Proceedings of the Royal Society A: Mathematical, Physical and Engineering Sciences, 472\(2189\), 20160117, 10.1098/rspa.2016.0117, 2016.](#)
- [Meyer, J., Voynova, Y. G., Van Dam, B., Luitjens, L., Daehne, D., & Thomas, H. Intertidal regions regulate seasonal coastal carbonate system dynamics in the East Frisian Wadden Sea. Biogeosciences, 22\(21\), 6255-6273, 10.5194/bg-22-6255-2025, 2025.](#)
- 820 [Meyerjürgens, J., Badewien, T. H., Garaba, S. P., Wolff, J. O., & Zielinski, O. A state-of-the-art compact surface drifter reveals pathways of floating marine litter in the German bight. Frontiers in Marine Science, 6, 58, 10.3389/fmars.2019.00058, 2019.](#)
- [Meyerjürgens, J., Ricker, M., Schakau, V., Badewien, T. H., & Stanev, E. V. Relative dispersion of surface drifters in the North Sea: The effect of tides on mesoscale diffusivity. Journal of Geophysical Research: Oceans, 125\(8\), e2019JC015925, 10.1029/2019JC015925, 2020.](#)
- 825 [Meyerjürgens, J., Ricker, M., Aden, C., Albinus, M., Barrelet, J., Freund, H., ... & Badewien, T. H. Sources, pathways, and abatement strategies of macroplastic pollution: an interdisciplinary approach for the southern North Sea. Frontiers in Marine Science, 10, 1148714, 10.3389/fmars.2023.1148714, 2023.](#)
- 830 [Molinari, R., & Kirwan, A. D. Calculations of differential kinematic properties from Lagrangian observations in the western Caribbean Sea. Journal of Physical Oceanography, 5\(3\), 483-491, 10.1175/1520-0485\(1975\)005<0483:CODKPF>2.0.CO;2, 1975.](#)
- 835 [Núñez-Riboni, I., & Akimova, A. Quantifying the impact of the major driving mechanisms of inter-annual variability of salinity in the North Sea. Progress in oceanography, 154, 25-37, 10.1016/j.pocean.2017.04.004, 2017.](#)
- [Liu, Y., Weisberg, R. H., Vignudelli, S., & Mitchum, G. T. Evaluation of altimetry-derived surface current products using Lagrangian drifter trajectories in the eastern Gulf of Mexico. Journal of Geophysical Research: Oceans, 119\(5\), 2827-2842, 10.1002/2013JC009710, 2014.](#)
- 840 [Loder, J. W., Drinkwater, K. F., Oakey, N. S., & Horne, E. P. Circulation, hydrographic structure and mixing at tidal fronts: the view from Georges Bank. Philosophical Transactions of the Royal Society of London. Series A: Physical and Engineering Sciences, 343\(1669\), 447-460, 10.1098/rsta.1993.0058, 1993.](#)

845 [Rudnick, D. L. On the skewness of vorticity in the upper ocean. *Geophysical Research Letters*, 28\(10\), 2045-2048, 10.1029/2000GL012265, 2001.](#)

[Ricker, M., Meyerjürgens, J., Badewien, T. H., & Stanev, E. V. Lagrangian methods for visualizing and assessing frontal dynamics of floating marine litter with a focus on tidal basins. *Chemical Oceanography of Frontal Zones*, 407-442, 10.1007/698_2021_812, 2021.](#)

850 [Schubert, R., Gula, J., Greatbatch, R. J., Baschek, B., & Biastoch, A. The submesoscale kinetic energy cascade: Mesoscale absorption of submesoscale mixed layer eddies and frontal downscale fluxes. *Journal of Physical Oceanography*, 50\(9\), 2573-2589, 10.1175/JPO-D-19-0311.1, 2020.](#)

855 [Shcherbina, A. Y., D'Asaro, E. A., Lee, C. M., Klymak, J. M., Molemaker, M. J., & McWilliams, J. C. Statistics of vertical vorticity, divergence, and strain in a developed submesoscale turbulence field. *Geophysical Research Letters*, 40\(17\), 4706-4711, 10.1002/grl.50919, 2013.](#)

860 [Shinki, M., Wendeborg, M., Vagle, S., Cullen, J. T., & Hore, D. K. Characterization of adsorbed microlayer thickness on an oceanic glass plate sampler. *Limnology and Oceanography: Methods*, 10\(10\), 728-735, 10.4319/lom.2012.10.728, 2012.](#)

[Simpson, J. H., Allen, C. M., & Morris, N. C. G. Fronts on the continental shelf. *Journal of Geophysical Research: Oceans*, 83\(C9\), 4607-4614, 10.1029/JC083iC09p04607, 1978.](#)

865 [Simpson, J. H., Brown, J., Matthews, J., & Allen, G. Tidal straining, density currents, and stirring in the control of estuarine stratification. *Estuaries*, 13\(2\), 125-132, 10.2307/1351581, 1990.](#)

870 [Stanev, E. V., Al-Nadhairi, R., Staneva, J., Schulz-Stellenfleth, J., & Valle-Levinson, A. Tidal wave transformations in the German Bight. *Ocean Dynamics*, 64\(7\), 951-968, 10.1007/s10236-014-0733-6, 2014.](#)

[Sun, Y. J., & Cho, Y. K. Tidal front and its relation to the biological process in coastal water. *Ocean Science Journal*, 45\(4\), 243-251, 10.1007/s12601-010-0022-3, 2010.](#)

875 [Tarry, D. R., Essink, S., Pascual, A., Ruiz, S., Poulain, P. M., Özgökmen, T., ... & D'Asaro, E. Frontal convergence and vertical velocity measured by drifters in the Alboran Sea. *Journal of Geophysical Research: Oceans*, 126\(4\), e2020JC016614, 10.1029/2020JC016614, 2021.](#)

880 [Tarry, D. R., Ruiz, S., Johnston, T. S., Poulain, P. M., Özgökmen, T., Centurioni, L. R., ... & Pascual, A. Drifter observations reveal intense vertical velocity in a surface ocean front. *Geophysical Research Letters*, 49\(18\), e2022GL098969, 10.1029/2022GL098969, 2022.](#)

[Thomas, L. N., & Lee, C. M. Intensification of ocean fronts by down-front winds. *Journal of Physical Oceanography*, 35\(6\), 1086-1102, 10.1175/JPO2737.1, 2005.](#)

885 [Thomas, L. N., Tandon, A., & Mahadevan, A. Submesoscale processes and dynamics. *Ocean modeling in an Eddying Regime. Geophysical Monograph Series*, 177, 17-38, 10.1029/177GM04, 2008.](#)

[Timko, P. G., Arbic, B. K., Hyder, P., Richman, J. G., Zamudio, L., O'Dea, E., ... & Shriver, J. F. Assessment of shelf sea tides and tidal mixing fronts in a global ocean model. *Ocean Modelling*, 136, 66-84, 10.1016/j.ocemod.2019.02.008, 2019.](#)

[Tippenhauer, S., Hoppmann, M., Gassen, L., Meyerjürgens, J., Physical oceanography during RV HEINCKE cruise HE626 \[dataset\]. PANGAEA, 10.1594/PANGAEA.963643, 2023.](#)

890 [Van Heijst, G. J. F. On the dynamics of a tidal mixing front. In *Elsevier oceanography series* \(Vol. 42, pp. 165-194\). Elsevier, 10.1016/S0422-9894\(08\)71045-6, 1986.](#)

[Vélez-Belchí, P., & Tintoré, J. Vertical velocities at an ocean front. *Scientia Marina*, 65\(S1\), 291-300, 10.3989/scimar.2001.65s1291, 2001.](#)

900 [Villa Castrillón, L., Ricker, M., Staneva, J., Meyerjürgens, J., Badewien, T. H., & Stanev, E. V. Relative dispersion and relative diffusivities in an ocean-wave coupled model of the North Sea. *Ocean Dynamics*, 74\(7\), 555-567, 10.1007/s10236-024-01619-6, 2024.](#)

905 [Wurl, O., Stolle, C., Van Thuoc, C., Thu, P. T., & Mari, X. Biofilm-like properties of the sea surface and predicted effects on air-sea CO₂ exchange. *Progress in Oceanography*, 144, 15-24, 10.1016/j.pcean.2016.03.002, 2016.](#)

[Wurl, O., Gassen, L., Badewien, T. H., Braun, A., Emig, S., Holthusen, L. A., ... & Ribas, M. R. HALOBATES: An Autonomous Surface Vehicle for High-Resolution Mapping of the Sea Surface Microlayer and Near-Surface Layer on Essential Climate Variables. *Journal of Atmospheric and Oceanic Technology*, 41\(12\), 1197-1211, 10.1175/JTECH-D-24-0021.1, 2024.](#)

910

[Zhang, Z., Liu, Y., Qiu, B., Luo, Y., Cai, W., Yuan, Q., ... & Tian, J. Submesoscale inverse energy cascade enhances Southern Ocean eddy heat transport. nature communications, 14\(1\), 1335, 10.1038/s41467-023-44386-6, 2023.](#)

[Zhao, C., Daewel, U., & Schrum, C. Tidal impacts on primary production in the North Sea. Earth System Dynamics, 10\(2\), 287-317, 10.5194/esd-10-287-2019, 2019.](#)